Computers and Fluids 221 (2021) 104902

Contents lists available at ScienceDirect

Computers and Fluids

journal homepage: www.elsevier.com/locate/compfluid

High-fidelity simulations of gravity currents using a high-order finite-difference spectral vanishing viscosity approach

Ricardo A.S. Frantz[a,b], Georgios Deskos[c], Sylvain Laizet[d,*], Jorge H. Silvestrini[a]

[a] School of Technology, Pontifical Catholic University of Rio Grande do Sul, Porto Alegre, Brazil
[b] DynFluid, Arts et Métiers, 151 Bd. de l'Hôpital, Paris 75013, France
[c] National Wind Technology Center, National Renewable Energy Laboratory, Golden, Colorado 80401, USA
[d] Department of Aeronautics, Imperial College London, London, SW7 2AZ, UK

ARTICLE INFO

Article history:
Received 25 November 2020
Revised 2 February 2021
Accepted 24 February 2021
Available online 3 March 2021

Keywords:
Large-eddy simulation
Direct numerical simulation
High-order finite-difference schemes
Spectral vanishing viscosity
Gravity current
Lock-exchange

ABSTRACT

This numerical work investigates the potential of a high-order finite-difference spectral vanishing viscosity approach to simulate gravity currents at high Reynolds numbers. The method introduces targeted numerical dissipation at small scales through altering the discretisation of the second derivatives of the viscous terms in the incompressible Navier-Stokes equations to mimic the spectral vanishing viscosity (SVV) operator, originally designed for the regularisation of spectral element method (SEM) solutions of pure advection problems. Using a sixth-order accurate finite-difference scheme, the adoption of the SVV method is straightforward and comes with a negligible additional computational cost. In order to assess the ability of this high-order finite-difference spectral vanishing viscosity approach, we performed large-eddy simulations (LES) of a gravity current in a channelised lock-exchange set-up with our SVV model and with the well-known explicit static and dynamic Smagorinsky sub-grid scale (SGS) models. The obtained data are compared with a direct numerical simulation (DNS) based on more than 800 million mesh nodes, and with experimental measurements. A framework for the energy budget is introduced to investigate the behaviour of the gravity current. First, it is found that the DNS is in good agreement with the experimental data for the evolution of the front location and velocity field as well as for the stirring and mixing inside the gravity current. Secondly, the LES performed with less than 0.4% of the total number of mesh nodes compared to the DNS, can reproduce the main features of the gravity currents, with the SVV model yielding slightly more accurate results. It is also found that the dynamic Smagorinsky model performs better than its static version. For the present study, the static and dynamic Smagorinsky models are 1.8 and 2.5 times more expensive than the SVV model, because the latter does not require the calculation of explicit SGS terms in the Navier-Stokes equations nor spatial filtering operations.

© 2021 Elsevier Ltd. All rights reserved.

1. Introduction

Gravity or density currents are commonly found in many physical processes involving the mixing between two fluids of different densities. They are driven by the density difference between a heavy fluid and a lighter ambient fluid. In nature, they can travel over long distances, up to hundreds of kilometres, in lakes, seas and oceans, with flow speeds of up to 20 m s^{-1} even on nearly flat floors [88]. The density difference can be caused by temperature, salinity or solid material in suspension. Examples of such flow phenomena are cold fronts, seafloor turbidity currents, snow avalanches, riverine plumes, pyroclastic lava flows, or anthropogenic like oil spills in the oceans and gas leaks in the atmosphere, and debris flows in urban areas from buildings collapse [1,99]. Understanding the physical mechanisms associated with these currents as well as the correct prediction of their main features are of great importance for practical and theoretical purposes. Gravity currents observed in nature are complex, very voluminous and are extremely challenging and costly to study. As a result, they have been mainly investigated in very simplified configurations such as the lock-exchange set-up (often in a channel configuration) where a sliding gate separates two volumes of fluid at rest; one volume contains a heavier fluid and the other a lighter one. When the gate is removed, differences in hydrostatic pressure generate a dense current moving along the bottom wall, while a neutrally buoyant current travels in the opposite direction along the top wall or free surface. Different phases of spreading have been identified for gravity currents in the lock-exchange set-up: (i) an acceleration phase where the current initially at rest reaches its

* Corresponding author.
E-mail address: s.laizet@imperial.ac.uk (S. Laizet).

https://doi.org/10.1016/j.compfluid.2021.104902
0045-7930/© 2021 Elsevier Ltd. All rights reserved.

maximum velocity, (ii) a slumping phase with a nearly constant front velocity, (iii) an inertial phase for which the buoyancy driving force is balanced by inertia and during which the current starts to decelerate, and (iv) a viscous phase for which the buoyancy driving force is balanced by viscosity [5,11,44,44]. Note that the last two phases are sometimes referred to as self-similar phases [44], although in some set-ups (e.g. short tanks or high concentrations) the viscous phase may not be observed. Conversely, in low Reynolds number cases (e.g. low concentration flows) the current may rapidly shift to a viscous dominated phase of spreading without experiencing an inertial phase (see [12] for details). Turbulent structures have also been identified as key components of the dynamics of gravity currents. Instabilities originating from the shear between the current and the ambient flow, as well as the near-wall high- and low-speed streaks, lead to well-known "lobe and cleft" structures located at the head of the current [29,42]. These coherent structures also enhance the exchange of mass and momentum between the ambient (lighter) and current (heavier) fluids, enabling mixing through turbulent entrainment [26,33,90,95].

To establish most of the existing knowledge on gravity currents, detailed experimental studies [8,9,21–23,37,64,65,74,79,92,95,96,98,114] and direct numerical simulations (DNS) [10,28,34,71–73,115] have been employed, primarily, in simplified configurations. DNS requires the flow field to be resolved adequately down to the smallest turbulent scales, where the energy of the flow is dissipated into heat. With such resolution requirements and current petascale supercomputers, DNS for gravity currents are limited to moderate Reynolds numbers, typically $Re \sim \mathcal{O}(10^4)$. DNS at higher Reynolds numbers are in theory possible but require a substantial amount of computational resources. On the other hand, large-eddy simulation (LES) is another widely used strategy to numerically study turbulent flows thanks to its ability to capture the main turbulent scales of the flow at a much lower cost than DNS, see [67,93] for an introduction.

LES has emerged recently as an appropriate tool to study the main features of gravity currents [18,66]. In LES, the mesh resolution is fine enough to capture the dynamics of most of the turbulent scales (up to a filter/mesh scale) while the contribution of the unresolved small scales is modelled. The traditional presentation of LES is based on the introduction of a low-pass filter used to separate the large-scale, resolved part of the flow from the residual, unresolved part, commonly referred to as the subgrid-scale (SGS) component . To this end, LES can provide answers to more-realistic, and higher-Reynolds-number problems, however, it relies on the adequate modelling of the subgrid-scale part as well as the energy transfers between the resolved and the subgrid scales which are both often parametrised through structural eddy viscosity models [35,68,100,109]. Inherently, the selection of the SGS model and the correct tuning of its parameters can dramatically affect the quality of the solution. Moreover, the interaction of the different LES parametrisations with the underlying numerical errors of the discretisation schemes was shown to be an important factor for accuracy [17,36,110]. To this end, implicit LES (iLES) methodologies, which utilise purely dissipative numerical schemes (e.g. upwinding schemes), have become viable alternative solutions in LES studies by combining numerical and physical parametrisations [7,39].

More recently, a new class of dissipation-inducing numerical schemes has emerged for high-order methods originating from the concept of spectral vanishing viscosity (SVV) proposed by Tadmor [102]. While the method was originally proposed for regularising spectral solutions of the Burger's equations, it was later employed to control high-wavenumber oscillations in the context of the incompressible Navier-Stokes equations [48,49,82,83]. Unlike the previously mentioned implicit LES schemes (which often rely on upwind schemes to add numerical dissipation), SVV adds dissipation exclusively to smaller scales, as defined by the mesh cut-off scale. A recent effort to employ the concept of SVV in higher-order compact finite difference schemes was proposed by Lamballais et al. [55], in which a numerical kernel was designed to manipulate numerical errors of the viscous term in the incompressible Navier-Stokes equations (via customised finite-difference schemes for the second derivatives). The strategy was initially aimed at controlling dispersive and aliasing errors at near cut-off scales. Due to its excellent performance, it was later extended and successfully applied to LES studies of isotropic turbulence (i.e. Taylor-Green vortex, [20]) as well as more complex flows (e.g. jets, wakes, etc.) [19,25,46].

For gravity currents, several LES studies have been performed in recent years, mainly based on an explicit SGS model approach. A review of LES of gravity currents was presented in [18] along with new results based on a dynamic Smagorinsky model and a non-dissipative viscous flow solver. This work discussed how the evolution and structure of gravity currents change when the Reynolds number is increased to values relevant in nature and environmental engineering applications. LES of lock-exchange in a channel set-up for a flatbed were performed in [76]. The LES solver in this study used a non-dissipative numerical scheme and was combined with the dynamic Smagorinsky model to account for the effect of the SGS stresses. The authors investigated the effect of the Reynolds number on the near-bed flow structure and the friction velocity distribution at the bottom of the channel, by performing simulations up to $Re \sim 250,000$. The Reynolds number dependence on mixing for lock-exchange gravity current was investigating in [81] using DNS and LES. Six different LES models were tested and it was found that all LES models provide an improvement with respect to DNS, however, it was not possible to identify a clear and consistent superior LES model.

Gravity currents past circular cylinders mounted above a wall were investigated in [38] using 2D and 3D LES with a focus on the force load on the cylinder and the behaviour of the friction velocity at the bottom wall near it. Their simulations considered Reynolds numbers in the range of $2,000 - 45,000$. LES were also employed by Tokyay et al. [104] and Tokyay et al. [106] to investigate the structure and evolution of a gravity current in a channelised lock-exchange set-up with a series of identical large-scale obstacles (dunes and square ribs) at the channel bottom. A dynamic approach similar to the dynamic Smagorinsky model was used for the unresolved scales (see [87] for more details). These studies looked into the effect of the roughness elements shape and height as well as the Reynolds number dependence on the temporal variation of the front velocity, mixing, and flow structure of the current. In [77,78] LES based on the dynamic Smagorinsky model were performed to study mixing and entrainment in unsteady gravity currents down a slope with different initial density difference and aspect ratio for the released volume. Data were compared with laboratory experiments, and the results showed a reasonable agreement. Ottolenghi et al. [80] examined the ability of Lattice-Boltzmann Method (LBM) to reproduce the fundamental features of lock-exchange gravity current by performing 2D and 3D LES at different Reynolds numbers. A peculiar modification of the basic LBM, equivalent to the Smagorinsky model, was employed using an effective collision relaxation time and obtained good agreement with laboratory data for Reynolds numbers up to $Re = 30,000$. LES of gravity currents in an axisymmetric lock-exchange set-up were performed in [45] for Reynolds numbers spanning several orders of magnitude. Their results reported hydraulic shocks for high Reynolds numbers which is consistent with results reported of [40] where a shallow-water equation solver was used. LES of lock-exchange gravity currents propagating over a mobile reach were presented in [52] to study the underlying mechanisms leading to sediment entrainment for different Reynolds numbers and grain sizes. To model the unresolved scales

in these two studies, the authors used the dynamic Smagorinsky with the constant evaluated using the Lagrangian procedure of [69] (see [2,91] for more details). The choice of the Lagrangian model in these studies was motivated by the absence of directions of homogeneity in the development of the currents. Density currents with a continuous release with a jet shape of dense fluid from a finite source down a sloping bed were studied recently in [15]. The authors studied the influence of the slope angle and stratification using LES based on a dynamic Smagorinsky model. Several approaches based on LES SGS models, detached eddy simulation (DES), delayed-detached eddy simulation (DDES), Launder-Reece-Rodi (LRR), and k-ϵ models were evaluated by Emami et al. [27] for gravity currents in the lock-exchange set-up. It was found that only DES and LES were able to capture the Kelvin-Helmholtz instability and the viscous phase of spreading. More recently, [86] used 200 LES based on the Smagorinsky model to provide a statistical analysis of a lock-exchange gravity current propagating over a 2% slope for a Reynolds number of 60,000, matching the experiments of [111]. It was found that the front velocity compares very well with analytical scaling laws, as well as experimental and numerical results previously reported. Likewise, the Kelvin-Helmholtz instabilities and the lobe and cleft instabilities at the front were correctly predicted. The authors also discussed the mechanisms of production and destruction of turbulence at the front of the current. The same authors investigated the influence of the mesh resolution in a LES context for a lock-exchange turbidity current [85]. The simulations were performed with a standard Smagorinsky model for a range of Reynolds numbers ranging from transitional currents to fully-developed ones. Spanwise two-point correlations were used to inform on the resolution needed to resolve the largest scales of the current and to check the placement of the LES filter size inside the inertial range.

In the present numerical study, the potential of the high-order finite-difference spectral vanishing viscosity approach of [55] is investigated to accurately simulate gravity currents at high Reynolds numbers. The method can introduce a targeted numerical dissipation at small scales through the discretisation of the second derivatives of the viscous term in the incompressible Navier-Stokes equations, mimicking a conventional spectral vanishing viscosity (SVV) approach. Based on sixth-order accurate finite-difference schemes, the method is straightforward to implement with a negligible computational extra cost by comparison to more conventional explicit LES models. The computational set-up and Reynolds number have been chosen so that they match the experimental measurements of [33]. In order to properly assess the potential of this SVV model, a large-scale DNS is also performed in order to compare quantities which are not available experimentally. To the best of our knowledge, this is one of the DNS with the highest Reynolds number for gravity currents in a lock-exchange set-up. LES with the well-known static and dynamic Smagorinsky models are also performed for comparison purposes. A novel framework for the energy budget is also introduced, in order to investigate the behaviour of the gravity current. One additional noverlty of the present study is that the LES are performed in the context of highly accurate finite-difference numerical methods. Such methods are desirable in a DNS context due to their ability to provide accurate results. However, in the context of LES, the sensitivity of high-order schemes at small scale can be counterproductive if there is a direct source of numerical errors, such as aliasing [51] at scales close to the mesh size. In particular, an explicit SGS model designed to reproduce the dissipation of the unresolved scales can be a strong source of numerical errors (the extra non-linearity introduced in the LES equations can produce additional aliasing errors).

The paper is organised as follows: the problem definition, the different LES approaches and the flow solver are described in Section 2. The comparison between the experiments of [33] and our DNS is presented in Section 3 followed by the LES results in Section 4. The paper is ended by a summary and conclusion in Section 5. A sensitivity study regarding the SVV approach is presented in Appendix A.

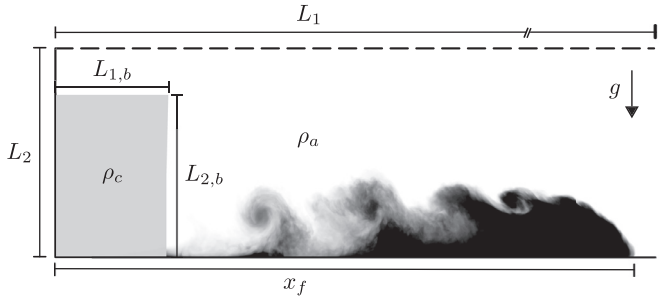

Fig. 1. 2D schematic view of a channelised lock-exchange set-up.

2. Problem definition and modelling approaches

2.1. Governing equations

To simulate gravity currents in a channelised lock-exchange set-up, we consider a finite volume release of a heavier fluid (density ρ_c) into a horizontal channel filled with lighter and initially calm ambient fluid (density ρ_a). Schematically, the flow configuration is presented in Fig. 1. The streamwise direction is x_1, the vertical direction is x_2 and the spanwise direction is x_3.

The heavier fluid is enclosed in a sub-domain of size $L_{1,b} \times L_{2,b} \times L_3$ in the computational domain of size $L_1 \times L_2 \times L_3$. At the initial time $t = 0$, the heavier fluid is released and the flow is driven purely by gravitational effects. To describe the dynamics of the gravity current mathematically, we make use of the unsteady incompressible Navier-Stokes equations coupled with a density transport equation. The coupling is achieved through a Boussinesq approximation of the gravitational term $(\rho_c - \rho_a)/\rho_a g e_i^g$ where g is the gravity acceleration and $e_i^g = (0, -1, 0)$ represents the unity vector acting in the direction of gravity. In the most generic, non-dimensional and unified (to accommodate both DNS and the various LES approaches) form, the governing equations can be written as

$$\frac{\partial u_i}{\partial x_i} = 0, \tag{1a}$$

$$\frac{\partial u_i}{\partial t} = -\frac{1}{2}\left(u_j \frac{\partial u_i}{\partial x_j} + \frac{\partial u_i u_j}{\partial x_j}\right) - \frac{\partial p}{\partial x_i} + \frac{1}{Re}\mathcal{D} + e_i^g Ri\rho, \tag{1b}$$

$$\frac{\partial \rho}{\partial t} = -u_j \frac{\partial \rho}{\partial x_j} + \frac{1}{Re \cdot Sc}\mathcal{Q} \tag{1c}$$

where u_i is the velocity vector field, p the pressure field and ρ is the density field. No reference to any filter is explicitly written in the equations. In a LES context, the unknowns u_i, ρ and p should be interpreted as the large-scale component of velocity, density and pressure.

The momentum diffusion term $\mathcal{D}$ can be expressed as

$$\mathcal{D} = \frac{\partial^2 u_i}{\partial x_j \partial x_j} \quad \text{for DNS (see section 2.2)},$$

$$\mathcal{D} = \frac{\partial}{\partial x_j}\left[(1 + Re \cdot \nu_t)\left(\frac{\partial u_i}{\partial x_j} + \frac{\partial u_j}{\partial x_i}\right)\right] \quad \text{for explicit LES (see section 2.3)},$$

$$\mathcal{D} = \frac{\partial^2 u_i}{\partial x_j \partial x_j} + \frac{\partial}{\partial x_j}\left(Q_c \star \frac{\partial u_i}{\partial x_j}\right) \quad \text{for SVV model (see section 2.4)}.$$

ν_t is the eddy viscosity computed by an explicit LES model. Q_c is a hyperviscous kernel used to construct the SVV operator

through a convolution operation ($\star$), as explained in Section 2.4. It will be shown that the hyperviscous kernel, although conceptualised purely in the spectral (wavenumber) domain, is meant for and applied only to the physical domain. The non-linear term of the momentum equation is computed in the skew-symmetric form for increased stability and to reduce aliasing errors [51], while the non-linear transport term is evaluated in its non-conservative form due to the use of different types of boundary conditions for the density field and velocity fields. The density diffusion term $\mathcal{Q}$ is defined in a similar fashion to the momentum diffusion term $\mathcal{D}$ (the operators for the derivatives in $\mathcal{Q}$ are the same as the operators in $\mathcal{D}$). Nonetheless, irrespective of the viscous/density diffusion operators formulation the non-dimensional governing equations are both expressed in terms of the Reynolds (Re) and Richardson (Ri) numbers. Their magnitude will ultimately change the physical characteristics of turbulence and therefore should be defined and computed with respect to the problems physical parameters. Thus, based on the initial density difference between the heavier and ambient fluid as well as the initial height $L_{2,b}$ of the heavy fluid column we apply an energy balance,

$$\frac{1}{2}\rho_c U_b^2 = \frac{1}{L_{2,b}}\int_0^{L_{2,b}} g(\rho_c - \rho_a)x_2 \mathrm{d}x_2, \tag{3}$$

to obtain a characteristic (or buoyancy) velocity scale $U_b = \sqrt{g' L_{2,b}}$, where $g' = g(\rho_c - \rho_a)/\rho_a$. Here we also assume for the energy balance that the entire dynamic energy of the initial set-up is converted to kinetic energy without any losses. This assumption although not valid (due to viscous effects), allows us to define global characteristic scales for the velocity and time variables. With this definition, the characteristic global Reynolds number can be expressed as

$$Re = \frac{U_b L_{2,b}}{\nu}, \tag{4}$$

where ν is the kinematic viscosity assumed to be the same for the two fluids. Similarly, the overall (bulk) Richardson number is given by

$$Ri = \frac{g' L_{2,b}}{U_b^2}. \tag{5}$$

Note that the choice of $L_{2,b}$ as characteristic length scale leads to $Ri = 1$. Additionally, we may define a dimensionless time scale $\tau = L_{2,b}/U_b$ which can be used to scale the time evolution of the gravity current. Finally, for the density transport the Schmidt (or Prandtl in the case of temperature) number $Sc = \nu/\kappa$ is defined based on a (constant) molecular diffusivity coefficient of the stratifying agent κ and is set to unity to avoid the use of finer meshes. It has been shown in [6] that the Schmidt number only weakly influences the structure and dynamics of gravity currents if the Reynolds number of the flow is large, $O(10^4)$ or more. On the contrary, gravity currents at low to moderate Reynolds numbers are dependant on the Schmidt number as the structure of the mixing region and the front velocities can be modified by diffusion effects.

Regarding boundary conditions and initial conditions, a no-slip boundary condition is applied for the velocity for $x_2 = 0$ while free-slip boundary conditions for $x_1 = 0$, $x_1 = L_1$ and $x_2 = L_2$ and periodic boundaries in the spanwise direction are imposed. For the density, a zero-flux ($\partial\rho/\partial x_i = 0$) boundary condition is applied everywhere ($x_1 = 0$, $x_1 = L_1$, $x_2 = 0$, $x_2 = L_2$), except in the spanwise direction where periodic boundary conditions are imposed. For the initial condition, the density concentration is prescribed by

$$\rho(x_1, x_2, x_3, t = 0) = 0.5 - 0.5\tanh\left[\delta_b(x_1 - L_{1,b})\right]. \tag{6}$$

In this work, the value $\delta_b = 20$ was found sufficient to avoid discontinuities in the derivatives while having a sharp enough profile to reproduce a virtual gate, even for the coarse mesh of the LES. Furthermore, the initial spatially-averaged velocity field is zero everywhere in the domain with white noise (corresponding to an initial kinetic energy of 1%) superposed to all velocity components at the gate position ($x = L_{1,b}$) in order to trigger flow instabilities (similar to the removal of the gate in an experiment).

2.2. Flow solver

The simulations in this study are carried out within the open-source, turbulence simulation framework `Xcompact3D`[1], designed for DNS and LES of incompressible and low-Mach number flows using a Cartesian mesh and high-order finite-difference schemes [3,53,54]. The incompressible flow solver within `Xcompact3D` is called `Incompact3d` and is based on sixth-order compact finite-difference schemes [53] for the spatial-discretisation and a fractional-step method using a third-order explicit Adams-Bashforth method for the temporal integration (other time schemes are available, depending on the flow configuration). Within the fractional-step method, the incompressibility condition is dealt with by directly solving a Poisson equation in spectral space using 3D Fast Fourier Transforms and the concept of the modified wavenumber [56]. The velocity-pressure mesh arrangement is half-staggered to avoid spurious pressure perturbations [53].

The simplicity of the mesh allows an easy implementation of a 2D domain decomposition based on pencils [54]. The computational domain is split into a number of sub-domains (pencils) which are each assigned to an MPI-process. The derivatives and interpolations in the x-direction (y-direction, z-direction) are performed in X-pencils (Y-pencils, Z-pencils), respectively. The 3D FFTs required by the Poisson solver are also broken down as a series of 1D FFTs computed in one direction at a time. Global transpositions to switch from one pencil to another are performed with the MPI command `MPI_ALLTOALL(V)`. The flow solvers within `Xcompact3D` can scale well with up to hundreds of thousands of MPI-processes for simulations with several billion mesh nodes [54]. The `Xcompact3D` framework has been used recently to perform DNS of Boussinesq gravity currents in various set-up and for a wide range of Reynolds numbers [28,29,34,62] and DNS of non-Boussinesq gravity currents [4]. Finally, further validation and verification studies of the code for the SVV model and the explicit LES models can be found in: [19,20,24,25,46,94].

2.3. Explicit SGS modelling

In this study, two reference explicit SGS models have been tested for comparison with the present SVV approach. Explicit LES relies on the direct modelling of the velocity and density subgrid-scale (SGS) stresses which appear in the momentum and density transport equations. To this end, the eddy viscosity ν_t and diffusivity κ_t variables are defined to approximate the subgrid-scale (SGS) stresses under the Boussinesq hypothesis,

$$\tau_{ij} = -2\nu_t S_{ij} \tag{7a}$$

$$q_j = -\kappa_t \frac{\partial \rho}{\partial x_j} \tag{7b}$$

where $S_{ij} = 0.5(\frac{\partial u_i}{\partial x_j} + \frac{\partial u_j}{\partial x_i})$ is the strain rate tensor. The eddy viscosity ν_t and eddy diffusivity κ_t are connected through the turbulent Schmidt number, $\kappa_t = \nu_t/Sc_t$. In our simulations the turbulent Schmidt number is set to unity as in the vast majority of nu-

[1] Freely available at github.com/xcompact3d/

merical studies of gravity currents. Alternatively, an empirical relationship to scale Sc_t as function of the coupling term can be sought (see [63,108]). The eddy viscosity can be modelled using a functional approach such as the ones afforded by the standard or dynamic Smagorinsky models [35,100]. Starting with the standard Smagorisnky model (SSM), the eddy viscosity is assumed to be proportional to the magnitude of the strain rate $|S|$ as well as a length scale $l_S = C_S\Delta$ which is proportional to the mesh scale $\Delta = \sqrt[3]{\Delta x_1 \Delta x_2 \Delta x_3}$ and an empirical coefficient C_S,

$$\nu_t = C_S^2 \Delta^2 |S|. \tag{8}$$

The empirical coefficient $C_S = 0.15$ is chosen for the simulations which is close to the theoretical value proposed by Lilly [59] for isotropic and homogeneous turbulence (a preliminary study confirmed that this value was the optimal value for the present set-up). The SSM has enjoyed popularity over the years thanks to its simple implementation, however, it has been found to behave over-dissipatively near walls and/or within turbulence-transition regions [67]. To this end, an alternative calculation of the eddy viscosity was proposed by Germano et al. [35] to adjust the Smagorinsky coefficient C_S in both space and time through a purely dynamic procedure. The model is based on Germano's algebraic identity [35] which relates subgrid/filter-scale stresses computed at two different levels,

$$\mathcal{L}_{ij} = T_{ij} - \widetilde{\tau_{ij}} = \widetilde{u_i u_j} - \widetilde{u}_i \widetilde{u}_j \tag{9}$$

where $T_{ij} = \widetilde{u_i u_j} - \widetilde{u}_i \widetilde{u}_j$ are the test filter level scale stresses, and $\widetilde{\tau_{ij}}$ are the subgrid-scale stresses filtered at the test filter scale. Note that $\widetilde{(\dots)}$ denotes the test filter level operation with $\widetilde{\Delta} = 2\Delta$. By assuming an eddy viscosity model such as the standard Smagorinsky just described in the previous paragraph and using Lilly's least-squares normalisation technique [60] we may obtain an expression for the DS eddy viscosity,

$$\nu_t = \frac{1}{2}\left\langle \frac{\mathcal{M}_{ij}\mathcal{L}_{ij}}{\mathcal{M}_{kl}\mathcal{M}_{kl}} \right\rangle_{x_3} \Delta^2 |S|, \tag{10}$$

where

$$\mathcal{M}_{ij} = 2\Delta^2 \widetilde{|S|S_{ij}} - 2\widetilde{\Delta}^2 |\tilde{S}|\tilde{S}_{ij}. \tag{11}$$

$\langle\rangle_{x_3}$ corresponds to an average in the spanwise direction (homogeneous direction of the current). The eddy viscosity and diffusivity are subsequently used in the momentum and density diffusion terms for their calculations as discussed in sub-Section 2.1.

2.4. Spectral vanishing viscosity

Spectral vanishing viscosity (SVV) used as a LES model has its roots in the concepts of spectral and hyper eddy viscosity [14,43,50]. The key idea of spectral eddy viscosity as discussed by Kraichnan [50] is that if one closely examines how eddy viscosity acts upon different wavenumber modes, then it can be shown that eddy viscosity must be allowed to depend upon the wavenumber magnitude. With this development, wavenumber dependent or simply spectral eddy viscosity (SEV) models were devised and applied in the spectral domain by Chollet and Lesieur [16], Lesieur and Rogallo [58], Métais and Lesieur [70]. For more information on SEV models, the reader is referred to the review of [57]. On the other hand, [43] undertook high-Reynolds number turbulence simulation by using the concept of hyperviscosity ($\nu\nabla^6\mathbf{u}$ instead of $\nu\nabla^2\mathbf{u}$) and observed no significant differences as far as the inertial region or the bottleneck phenomenon [30] of the energy spectra is concerned, while significantly reducing their mesh resolution. Spectral vanishing viscosity combines the two models by conceptualising eddy viscosity in the spectral domain but applying it in the physical domain in a form similar to hyperviscosity. The SVV operator is implemented by multiplying the Fourier coefficients of the velocity field, u_i, with the Fourier coefficients of a smooth SVV kernel Q_c,

$$\nu_0 \frac{\partial}{\partial x_j}\left[Q_c \star \frac{\partial u_i}{\partial x_j} \right] = -\nu_0 \sum_{k_0 \le |k| \le k_c} k^2 \widehat{Q}_c \widehat{u}_k e^{ikx_k} \tag{12}$$

where ν_0 is the magnitude of SVV, $\star$ denotes a convolution operator and k_n and k_0 are the cut-off wavenumber (defined by the mesh size) and the wavenumber above which SVV is activated, respectively. The Fourier coefficients of the smooth kernel, may be expressed via an exponential function following [48]

$$\widehat{Q}_c(k) = \exp\left[-\left(\frac{k - k_c}{\gamma k_c - k} \right)^2 \right], \quad \text{for} \quad k \ge \gamma k_c. \tag{13}$$

This kernel is different from the original Heaviside function proposed by Tadmor [102] and it can be argued that it exhibits a number of advantages. It should be noted that one may easily change the shape of the kernel by changing the value of γ. With increasing γ the SVV kernel becomes steeper and thus affects only the smaller length-scales. On the other hand, as γ becomes smaller, the range of the scales affected by eddy viscosity is broadened, which better resembles the behaviour of a spectral eddy viscosity model. For our study, a value $\gamma = 0.3$ is chosen as it is the value which gives the closest match with the exponential model of [48]. The effect of parameter γ is shown in Fig. 2 where the wavenumber range in which the SVV viscosity is applied (and its respective amplitude) appears to decrease with increasing γ. The implementation of the discrete SVV kernel in the framework of high-order compact finite-differences is discussed in sub-Section 2.5.

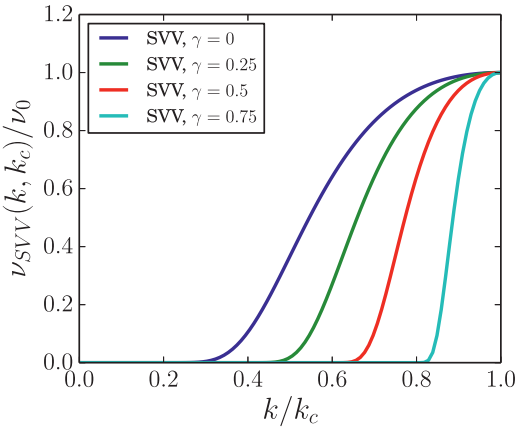

Fig. 2. Normalised SVV kernels as a function of the normalised wavenumber k/k_c for different γ.

Compared to the hyperviscosity model, e.g. [43], spectral vanishing viscosity differs in that the amount of dissipation added to the solution is active only after a particular wavenumber and therefore does not affect large energetic scales (triad interaction between the resolved scales). Finally, regarding determining the magnitude of eddy viscosity ν_0, most previous studies have relied on a "trial-and-error" approach, and an optimum value is often selected based on a better agreement with the reference data. In recent work, however, [20] determined the magnitude of SVV in the context of isotropic turbulence using Pao's equilibrium energy spectrum. This approach will be considered here together with several other values for ν_0. An alternative approach is that of using the dynamic SVV model [25,49] in which the spectral eddy viscosity is scaled locally by the magnitude of the strain-rate tensor. Such an approach for gravity currents was tested in a preliminary study and did not provide an improvement in the quality of the solution when compared to the approach used in the present work.

2.5. Implementation of the SVV and filtering operators using high-order finite-difference schemes

The high-order strategy considered in this study for accuracy is based on finite-difference schemes implemented on a Cartesian mesh. The main advantages of this specific numerical configuration being its simplicity and efficiency [53,56]. The second order derivatives in the momentum diffusion term $\mathcal{D}$ and density diffusion term $\mathcal{Q}$ are based on a compact (implicit) finite-difference scheme, with a 3–9 node stencil:

$$\alpha f''_{i-1} + f''_i + \alpha f''_{i+1} = a\frac{f_{i+1}-2f_i+f_{i-1}}{\Delta x^2} + b\frac{f_{i+2}-2f_i+f_{i-2}}{4\Delta x^2} + c\frac{f_{i+3}-2f_i+f_{i-3}}{9\Delta x^2} + d\frac{f_{i+4}-2f_i+f_{i-4}}{16\Delta x^2}, \tag{14}$$

where $f_i = f(x_i)$ and $f''_i = f''(x_i)$ represent discrete approximations of the function $f(x)$ and its second derivative $f''(x)$ at nodes $x_i = (i-1)\Delta x$ where Δx is the uniform mesh spacing. Such schemes have a so-called quasi-spectral behaviour [56] due to their capabilities to represent accurately a wide range of scales. A Fourier analysis for such schemes, for which $f(x)$ and $f''(x)$ are decomposed and analysed in the Fourier space ($\hat{f''}_l = -k^2\hat{f}_l$, where $\hat{f}_l$ and $\hat{f''}_l$ are Fourier coefficients and k^2 are the associated wavenumbers), can provide an effective way to quantify their resolution characteristics [56]. A Fourier analysis of the above scheme yields a modified wavenumber,

$$k''(k) = \frac{2a[1-\cos(k\Delta x)] + \frac{b}{2}[1-\cos(2k\Delta x)] + \frac{2c}{9}[1-\cos(3k\Delta x)] + \frac{d}{8}[1-\cos(4k\Delta x)]}{\Delta x^2[1+2\alpha\cos(k\Delta x)]}. \tag{15}$$

which depends on coefficients (α, a, b, c, d). These coefficients are determined based on a desired formal accuracy of the second derivative (e.g fourth- or sixth-order accuracy) by satisfying the following equations in an accumulating order,

$$a + b + c + d = 1 + 2\alpha \quad \text{(second order)} \tag{16a}$$

$$a + 2^2 b + 3^2 c + 4^2 d = \frac{4!}{2!}\alpha \quad \text{(fourth order)} \tag{16b}$$

$$a + 2^4 b + 3^4 c + 4^4\ d = \frac{6!}{4!}\alpha \quad \text{(sixth order)} \tag{16c}$$

$$a + 2^6 b + 3^6 c + 4^6 d = \frac{8!}{6!}\alpha \quad \text{(eight order)} \tag{16d}$$

$$a + 2^8 b + 3^8 c + 4^8 d = \frac{10!}{8!}\alpha \quad \text{(tenth order)}. \tag{16e}$$

For example, by satisfying all equations up to (16c) the coefficients are calculated to be equal to $\alpha = 2/11$, $a = 12/11$, $b = 3/11$ and $c = d = 0$ and the approximation is sixth-order accurate [56]. The rationale here is to obtain the desired accuracy with the smallest possible stencil while keeping the implicit character of the scheme, hence the choice of $c = d = 0$. Following however [55] a discrete SVV operator may be constructed by allowing k'' to mimic the behaviour of the analytical model of [48] for which the extra numerical viscosity can be expressed as

$$\frac{\nu_{SVV}(k, k_c)}{\nu_0} = \begin{cases} 0 & \text{if } k < 0.3k_c \\ \exp\left[-\left(\frac{k_c - k}{0.3k_c - k}\right)^2\right] & \text{if } 0.3k_c \le k \le k_c, \end{cases} \tag{17}$$

where $k_c = \pi/\Delta x$ is the mesh cut-off wavenumber. It is possible to customise the finite-difference scheme (14) to mimic this SVV operator while maintaining a sixth-order accuracy by satisfying all equations up to (16c). However two more constrains need to be added to the system of equations at $k = k_m = 2/3k_c$ and $k = k_c$ so that

$$k''(k_c) = \left(1 + \frac{\nu_0}{\nu}\right)k_c^2, \tag{18a}$$

$$k''(k_m) = \left(1 + 0.437\frac{\nu_0}{\nu}\right)k_m^2. \tag{18b}$$

where ν_0/ν is set to be the desired ratio between the SVV magnitude ν_0 and the background kinematic viscosity ν. Equations (18a) and (18b) are determined by requiring $-\nu k''(k) = -[\nu + \nu_{SVV}(k)]k^2$ at both $k = k_c$ and $k = k_m = 2/3k_c$. With these two constraints and to keep a sixth-order accuracy, the set of coefficients for the scheme (14) can be expressed as,

$$\alpha = \frac{1}{2} - \frac{320k''_m\Delta x^2 - 1296}{405k''_c\Delta x^2 - 640k''_m\Delta x^2 + 144} \tag{19a}$$

$$a = -\frac{4329k''_c\Delta x^2/8 - 32k''_m\Delta x^2 - 140k''_c\Delta x^2 + 286}{405k''_c\Delta x^2 - 640k''_m\Delta x^2 + 144} \tag{19b}$$

$$b = \frac{2115k''_c\Delta x^2 - 1792k''_m\Delta x^2 - 280k''_c\Delta x^2 + 1328}{405k''_c\Delta x^2 - 640k''_m\Delta x^2 + 144} \tag{19c}$$

$$c = -\frac{7695k''_c\Delta x^2/8 + 288k''_m\Delta x^2 - 180k''_c\Delta x^2 - 2574}{405k''_c\Delta x^2 - 640k''_m\Delta x^2 + 144} \tag{19d}$$

$$d = \frac{198k''_c\Delta x^2 + 128k''_m\Delta x^2 - 40k''_c\Delta x^2 - 736}{405k''_c\Delta x^2 - 640k''_m\Delta x^2 + 144}, \tag{19e}$$

where k''_c is the expected value of k'' at the mesh cut-off wavenumber and k''_m is the expected value of k'' at 2/3 of the mesh cut-off wavenumber.

The resulting discrete "hyper-viscous" operator contains both the SVV and viscous parts. Thus, the actual behaviour of the discrete SVV operator in the wavenumber space can be found only after we separate the viscous part ($-\nu k^2$), from the hyper-viscous part $-\nu k''$, and obtain the actual discrete spectral vanishing viscosity $\nu''(k)$ via

$$-\nu''(k)k^2 = -\nu(k'' - k^2). \tag{20}$$

A plot of the final discrete SVV operator is shown in Fig. 3 together with the analytical function of [48]. The theoretical "modified" wavenumber kernel is equal to $k'' = (1 + \nu''(k)/\nu)k^2$.

The discrete SVV kernel is found to be a satisfactory approximation of the analytical operator of [48] for the whole wavenumber range with only small deviations at the near cut-off $0.75k_c < k < k_c$ and half cut-off $0.4k_c < k < 0.6k_c$ wavenumbers where only small differences in the relative magnitude are observed ($\sim 10-20\%$). These differences are not expected to alter either the quality of our results or our conclusions.

Regarding the filtering operator required by the dynamic Smagorinsky model, a discrete test filter is constructed using compact finite differences. The filtered fluid property $\hat{f}_i$ is computed with a $3-9$ node stencil,

$$\alpha\hat{f}_{i-1} + \hat{f}_i + \alpha\hat{f}_{i+1} = af_i + \frac{b}{2}(f_{i+1} + f_{i-1}) + \frac{c}{2}(f_{i+2} + f_{i-2}) + \frac{d}{2}(f_{i+3} + f_{i-3}), \tag{21}$$

where the coefficients α, a, b, c, d are set to satisfy sixth-order accuracy which is consistent with the truncation error of all other spatial discrete operators. Hence, the discrete filter coefficients are found to be equal to $a = 0.0625(11 + 10\alpha)$, $b = 0.0312532(15 + 34\alpha)$, $c = -0.0625(3 - 6\alpha)$, $d = 0.03125(1 - 2\alpha)$, where $\alpha \in [-0.5, 0.5]$ is a free user-defined parameter. In our study

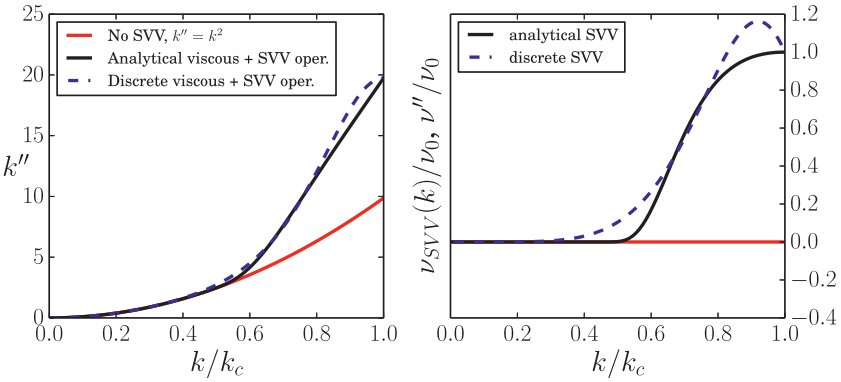

Fig. 3. Modified wavenumber k'' and the spectral vanishing viscosity (SVV) kernel for the analytical operator of [48] and the proposed operator normalised by the SVV magnitude ν_0.

we have chosen to use $\alpha = 0$ to approximate a Gaussian filter in the wavenumber space, aiming at an effective filter size equal to $\tilde{\Delta} \approx 2\Delta$. Finally, it is noteworthy that for non-periodic boundaries and for stability reasons, filtering at the first mesh node is avoided.

2.6. Energy budget framework

A complete energy budget for gravity currents in the lock-exchange set-up can be extracted from the governing equations and density transport equation, see [73] and [28]. The energy budget can be used to better understand gravity currents by investigating the temporal evolution of the potential energy, kinetic energy and associated energy transfer mechanisms. In the present study, the conceptual framework of [112], based on available and background potential energy [61], is adapted to lock-exchange gravity currents. Such a framework, which has been widely used for stratified flows [31,33,75,77,84], can distinguish the stirring (a large-scale reversible process) and mixing (a small-scale irreversible process) features of a gravity current. As explained in the experimental reference study of [33], this approach can explicitly capture the changes in potential energy due to adiabatic processes, which transport fluid elements without molecular mass or heat transfer (stirring), from changes due to diabatic processes (mixing). The energy budget will be used for comparison with the experimental work of [33] and to assess the performance of the LES models.

Overall, the total energy $\mathcal{T}$ for the gravity current is equal to

$$\mathcal{T}(t) = \mathcal{P}_a(t) + \mathcal{P}_b(t) + \mathcal{K}(t) + \mathcal{I}(t), \tag{22}$$

where $\mathcal{P}_a$ is the available energy, $\mathcal{P}_b$ is the background energy, $\mathcal{K}$ is the total kinetic energy and $\mathcal{I}$ is the internal energy. The total potential energy $\mathcal{P}$ is defined as

$$\mathcal{P}(t) = \int_V [\rho(x_1, x_2, x_3, t)x_2]\mathrm{d}V, \tag{23}$$

where the integral is taken over the full computational domain. The background potential energy $\mathcal{P}_b$ is defined as the minimum potential energy attainable through an adiabatic redistribution of the density field. It can be expressed as a function of time as

$$\mathcal{P}_b(t) = \int_V \rho^*(x_1, x_2, x_3, t)x_2\mathrm{d}V. \tag{24}$$

$\rho^*(x_1, x_2, x_3, t)$ is the density field redistributed in the minimal energy state (see as an example Fig. 2 of [33]). In our simulations, $\mathcal{P}_b$ is approximated from the 3D density snapshots with the pdf method, sampled with a computationally inexpensive empirical cumulative distribution function (e.c.d.f.), following an approach introduced by Oezgoekmen et al. [75], Tseng and Ferziger [107]. The available potential energy $\mathcal{P}_a$ is defined as the difference between the total potential energy $\mathcal{P}$ and the background potential energy $\mathcal{P}_b$

$$\mathcal{P}_a(t) = \mathcal{P}(t) - \mathcal{P}_b(t), . \tag{25}$$

Two routes are available for the conversion of available potential energy $\mathcal{P}_a$ to background potential energy $\mathcal{P}_b$. The first route is associated with stirring. The total kinetic energy $\mathcal{K}$, defined as

$$\mathcal{K}(t) = \frac{1}{2}\int_V \left[u_1^2(x_1, x_2, x_3, t) + u_2^2(x_1, x_2, x_3, t) + u_3^2(x_1, x_2, x_3, t)\right]\mathrm{d}V. \tag{26}$$

can be modified via reversible vertical buoyancy flux, defined as

$$\varpi(t) = \int_V \rho(x_1, x_2, x_3, t)u_2(x_1, x_2, x_3, t)\mathrm{d}V. \tag{27}$$

Changes in total kinetic energy $\mathcal{K}$ can indeed be associated with changes in dissipation (the total kinetic energy will eventually be transformed in heat via dissipation), which will affect the internal energy and ultimately the background energy via density diffusion. The total viscous dissipation can be explicitly computed as

$$\epsilon(t) = \frac{1}{Re}\int_V \frac{\partial u_i(x_1, x_2, x_3, t)}{\partial x_j}\frac{\partial u_i(x_1, x_2, x_3, t)}{\partial x_j}\mathrm{d}V, \quad i, j = 1, 2, 3. \tag{28}$$

while density diffusion can be defined as

$$\Phi(t) = \frac{1}{ReSc}\int_V x_2\frac{\partial^2 \rho(x_1, x_2, x_3, t)}{\partial x_i^2}\mathrm{d}V \qquad i = 1, 2, 3. \tag{29}$$

Viscous dissipation and density diffusion are unidirectional energy mechanisms which act as source and sink of the internal energy, respectively. The internal energy $\mathcal{I}$ can be evaluated as

$$\mathcal{I}(t) = \int_0^t [\epsilon(t) - \Phi(t)]\mathrm{d}t. \tag{30}$$

The second route for the conversion of available potential energy $\mathcal{P}_a$ to background potential energy $\mathcal{P}_b$ is a direct route, known as irreversible dyapicnal mixing. The term dyapicnal refers to the fact that mixing is a diffusive process across interfaces of different densities (also known as diapycnal surfaces), hence this route is only available in stratified flows as explained in [112]. In the current framework, irreversible dyapicnal mixing is defined as an irreversible energy transfer mechanism acting towards smoothing gradients of ρ (directly increasing the background potential energy $\mathcal{P}_b$). Following the work of [112], irreversible dyapicnal mixing can be simply defined as the time derivative of

$$\varrho(t) = \dot{\mathcal{P}}_b(t). \tag{31}$$

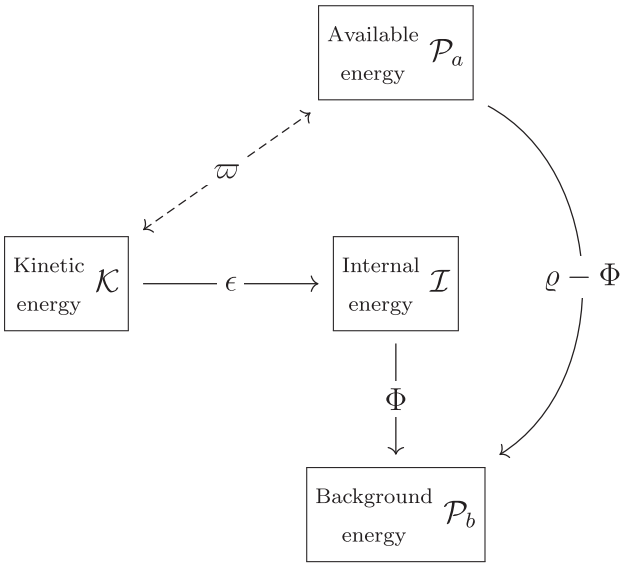

Fig. 4. New energy budget framework for gravity currents in a lock-exchange set-up.

The energy budget framework is presented in Fig. 4, with the distribution of energy among the different terms. Note finally that in the next sections, the energy budget is normalised by the total potential energy at the start of the simulation $\mathcal{P}(t=0) = \mathcal{T}(t=0)$.

3. DNS validation against experimental data

The laboratory experiment number 6 of [33] (EX6) has been selected as a reference for comparison with the simulations. It consists of a dense solution (with $g' = 12$ cm s^{-2}) made from sugar and water which is placed behind a plastic lock in a 2.4 m $\times$ 0.5 m $\times$ 0.1 m tank filled with tap water. The domain size for the simulations is equal to $L_1 \times L_2 \times L_3 = 12 \times 1 \times 0.5$ whereas the initial reservoir $L_{1,b} \times L_{2,b} \times L_3 = 1 \times 1 \times 0.5$. The Reynolds number is equal to 31,000. It should be noted that in the present set-up and reference experiment $L_2 = L_{2,b}$. Only limited experimental data are available for comparison with the present simulations: (i) instantaneous spanwise-averaged density fields at regular time intervals, (ii) the temporal evolution of the front position and associated front velocity (extracted from the movies provided with the article); (iii) the evolution of the dilution based on normalised subareas of specific density thresholds; and (iv) the evolution of available and background potential energy. Hence, the strategy here is to first perform a DNS, compare the results with the available experimental data and then assess the performance of the LES models with the DNS data. Note that the Reynolds number in EX6 is large enough for a LES approach and it remains computationally reachable for a DNS.

For a DNS, all turbulent scales are supposed to be adequately resolved down to the mesh level. Such requirement, however, imposes certain restrictions on the spatial resolution. According to Pope [89] the mesh spacing for a DNS (in physical space) should be $\Delta x \approx 2.1\eta_K$ where $\eta_K = (\nu^3/\varepsilon_K)^{1/4}$ is the Kolmogorov scale, representative of the smallest scale in a turbulent flow, where viscosity dominates and the turbulent kinetic energy is dissipated into heat. In the definition of η_K, ε_K is considered as the averaged rate of dissipation of turbulence kinetic energy per unit mass. Note that the computation of ε_K is not straightforward in the context of gravity currents: the flow is transitional, evolving from a laminar to a highly-turbulent state; there is a significant anisotropy due to stratification; the flow is inhomogeneous due to the presence of walls and there are no homogeneous spatial directions for averaging (except the spanwise direction for channelised currents). Finally, the recommendation from Pope [89] did not take into account the accuracy of the numerical methods. It is now well-established that, in terms of accuracy and computational efficiency, the most spectacular gain is obtained using spectral methods based on Fourier or Chebyshev representation [13]. In particular, highly accurate finite-difference numerical methods, with quasi-spectral properties, are desirable in a DNS context due to their ability to provide flexibility for the boundary conditions (as opposed to purely spectral methods) and accurate results with a moderate number of mesh nodes when compared to more conventional low-order schemes.

In almost all published DNS studies of gravity currents, no estimate of the Kolmogorov scale is provided, with usually very little information on mesh requirement for a given Reynolds number other than a mesh convergence study. Härtel et al. [41] suggested that the number of mesh nodes required to achieve adequate resolution depends on the steepness of the initial profile for the concentration field at the gate (in a channelised lock-exchange set-up, see δ_b in Eq. 6). The authors also recommended using the same resolution in the streamwise and vertical directions in the middle of the channel while a much more refined mesh is needed close to the bottom wall to allow for an adequate resolution of the developing boundary layer. Zgheib et al. [115] justified their spatial resolution by observing between 4 and 6 decades of decay in the streamwise-spectra of particle-volume fraction at various times. They also claimed to have similar decay for other quantities and vertical-spectra and spanwise-spectra. Similar arguments were used in [11] to justify the spatial resolution for DNS of axisymmetric gravity currents. In [28,29], the authors looked at the energy budget and in particular at the total energy, which is supposed to be conserved if all the turbulent scales are modelled properly. If the smallest scales of the flow (the dissipative ones) are not resolved, then an accumulation of energy would appear at the mesh resolution level, and the total energy would not be conserved. Note that this accumulation of energy would also be visible on energy spectra.

The DNS is discretised with $n_1 \times n_2 \times n_3 = 4097 \times 769 \times 257$ mesh nodes and a time step of $\Delta t = 2 \times 10^{-4}$. Note that the mesh is not refined closed to the bottom wall in the vertical direction. This spatial resolution has been chosen after a mesh refinement study to make sure that the solution is independent of the mesh resolution. Expressed in wall viscous units, it corresponds to a maximal resolution of $\Delta^+_{x_{1_{\max}}} \approx 1$, $\Delta^+_{x_{2_{\max}}} \approx 0.5$ and $\Delta^+_{x_{3_{\max}}} \approx 1$. Those values have been obtained by calculating the maximum value of the spanwise-averaged wall shear velocity at each time step. The DNS is performed with 8192 computational cores on the UK Supercomputing facility ARCHER. The spatial resolution required to capture the smallest scales of the flow adequately was checked by looking at the temporal evolution of the ratio between the spatial resolution and the largest Kolmogorov scale for each time step, see Fig. 5. The average rate of dissipation of turbulence kinetic energy per unit mass ε_K is evaluated at each time step using the following expression

$$\varepsilon_K = \frac{1}{Re}\frac{\partial u_i'}{\partial x_j}\frac{\partial u_i'}{\partial x_j}, \qquad i,j = 1,2,3 \tag{32}$$

where the fluctuating velocities u_i' have been obtained by removing the spanwise-averaged mean velocity at each time step. It can be seen in figure 5 that in the vertical direction, the condition $\Delta x_2/\eta_K \leq 2$ is always satisfied while $\Delta x_3/\eta_K \leq 3$ and $\Delta x_1/\eta_K \leq 5$ are satisfied in the spanwise and streamwise directions, respectively. It should be noted that for more than 90% of the simulation, $\Delta x_i/\eta_K \leq 2$, and the largest η_K are located in the head of the gravity current, at the early stages of the simulations, close to the peak of total kinetic energy, see Fig. 15. It is also important to reiter-

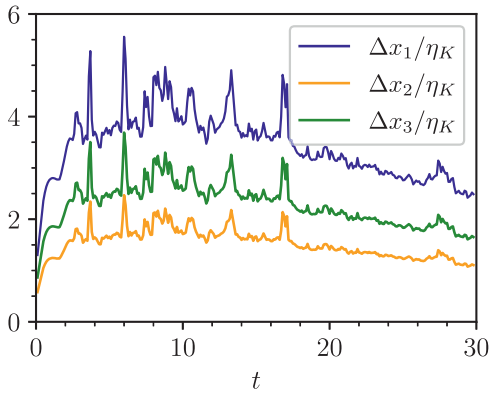

Fig. 5. Temporal evolution of the spatial resolution with respect to the Kolmogorov scale for the present DNS.

ate that the well-know recommendation from [89] ($\Delta x_i/\eta_K \approx 2.1$) about resolution requirements does not take into account the order of the numerical schemes. High-order schemes such as the ones used in the present study are able to capture more small scales at a given resolution than low-order schemes. Fig. 5 suggests that the mesh resolution is fine enough to take into account the smallest features of the current and a good comparison with the experimental data can be expected. Furthermore, as an extra check for the resolution requirement, Fig. 15a shows that the total energy in the DNS is perfectly conserved, confirming that the spatial resolution is adequate for the present study.

Fig. 6 shows the evolution of the spanwise-averaged density field at $t = 12.4$ and $t = 24$ for the DNS and EX6. Overall, it can be seen that the experimental current and the numerical current are almost identical, with a similar shape, and they seem to be evolving at the same speed. The well-known Kelvin-Helmholtz billows can clearly be seen, especially for the DNS. Few differences can be observed at the interface between the current and its ambient, with a clearer interface for the experiment. This could be attributed to the difficulty in the experiment to capture low thresholds for the density field, as reported in [33]. The head of the current is also more pronounced in the simulation (darker red) for $t = 12.4$, suggesting that the current might carry more energy in the DNS than in the experiment. This can be related to the noisy removal of the gate in the experiment which might have consumed extra energy. However, the opposite trend can be observed for $t = 24$, with a more diffuse head for the DNS. It might be related to a more intense mixing activity at the interface for the DNS, which could consume more energy than in the experiments.

To track the evolution of the front position $x_f(t)$ in the DNS, a simple reverse search is performed on the quantity $\bar{\rho}$ defined as

$$\bar{\rho}(x_1, t) = \int_0^{L_2} \int_0^{L_3} \rho(x_1, x_2, x_3, t) \mathrm{d}x_2 \mathrm{d}x_3, \tag{33}$$

The streamwise position of the front of the current $x_f(t)$ is defined as the first position where $\bar{\rho}(x_1, t) > 0.01$ (starting from the end of the computational domain in the streamwise direction). The associated front velocity $u_f(t)$ is evaluated by calculating the derivative of $x_f(t)$ with respect to time. Fig. 7a shows the temporal evolution of $x_f(t)$ for both EX6 and the DNS. The experimental values have been extracted from Fragoso et al. [33] by using 32 equally-spaced frames from the video provided with the article. A specific modulation has been used to make sure that the aspect ratio of the video is the same as in the DNS. An excellent agreement between the experiment and the DNS is obtained for the location of the front position. Note that t_s corresponds to the end of the slumping phase and t_i to the end of the inertial phase.

The temporal evolution of the front velocity is presented in Fig. 7b. For the DNS, the acceleration phase (in which the current initially at rest reaches its maximum velocity) peaks at $t \approx 1.5$ and is followed by a small deceleration phase up to $t \approx 4$. Note that the acceleration phase for the experiment cannot be captured properly due to the coarse temporal resolution from the video and the large perturbations generated by the manual removal of the gate. After $t \approx 4$ and up to $t_s = 14$, both sets of data indicate that the front velocity is nearly constant, corresponding to the slumping phase, with $u_{f,s} = 0.44$. The front velocity then starts to decrease first at a slow rate (inertial phase, up to $t = 21$), then at a fast rate (viscous phase). The current then hit the end of the computational domain for the DNS and the wall at the end of the water tank for the experiment for $t_w \approx 27$. Overall, numerical and experimental data for the front velocity are in good agreement with each other. Several theoretical and empirical models have been proposed to predict the front velocity during the inertial and viscous phases, where the current decelerate following power-law decays, with $u_f \propto t^{-\alpha}$, see [11,44]. For the inertia phase, it was suggested that $\alpha = 1/3$ and for the viscous phase that $\alpha = 4/5$, values recovered here for both numerical and experimental data as seen in Fig. 7b.

The dilution of the heavy fluid into the light ambient fluid was carefully investigated in [33] by counting over time areas of the current greater than arbitrary thresholds (using density colour maps for the spanwise-averaged density field). In our DNS, in a similar fashion to [73], a subarea A^{ρ_1}, where ρ exceeds a certain threshold ρ_1, can be defined for the spanwise-averaged density field

$$A^{\rho_1}(t) = \int_A (\langle \rho(x_1, x_2, t) \rangle_{x_3} \geq \rho_1) \mathrm{d}A. \tag{34}$$

Fig. 8a shows the temporal evolution of $A^{\rho_1}/A_0^{\rho_1}$ (where $A_0^{\rho_1} = A^{\rho_1}(t = 0)$) for thresholds $\rho_1 = 0.02, 0.5, 0.8, 0.92$. The initial density field is zero everywhere, except in the reservoir for which it is equal to 1. In an idealised mixing scenario where the reservoir and the ambient have the same volume, the density field would eventually be equal to 0.5 everywhere (corresponding to a perfect mixing). It is therefore natural to expect $A^{\rho_1}(t)/A_0^{\rho_1}$ to go above/below 1 for thresholds below/above 0.5. In practice, and due to the lock-exchange set-up in the present work, this might not be exactly the case. It also should be noted that the error margin is quite large in the experiments due to the difficulties associated with capturing certain density levels with advanced optical techniques, as mentioned in [33]. Furthermore, the manual removal of the gate in the experiments is producing more perturbations than its numerical counterpart based on a numerical white noise (the reader can have a look at the video of the experiments provided with the article). It is therefore anticipated that more stirring and mixing would occur in the experiments soon after removing the gate. As a result, a small time delay (intrinsic to the threshold) is expected: large thresholds for $A^{\rho_1}/A_0^{\rho_1}$ will decay earlier and small thresholds for$A^{\rho_1}/A_0^{\rho_1}$ will increase earlier, by comparison to the simulations. Thresholds around 0.5 should not be affected.

A convincing agreement between the experimental and numerical data can be observed for the threshold 0.5. As expected, the large experimental thresholds for $A^{\rho_1}/A_0^{\rho_1}$ are decaying earlier than the ones in the simulation, however the rate of decay for both the experiment and the simulation are the same for $\rho_1 = 0.8$ and $\rho_1 = 0.92$. It confirms that without a noisy removal of the gate in the experiment or with a noisier artificial perturbation in the simulation, the blue and yellow lines would be on top of the blue and yellow symbols. For the lowest threshold, the agreement between the experiment and the simulation is not so good which confirm that capturing properly very low thresholds in the experiment is challenging due to margin of error of the camera, as mentioned by Fragoso et al. [33]. The present results also confirm that accurate

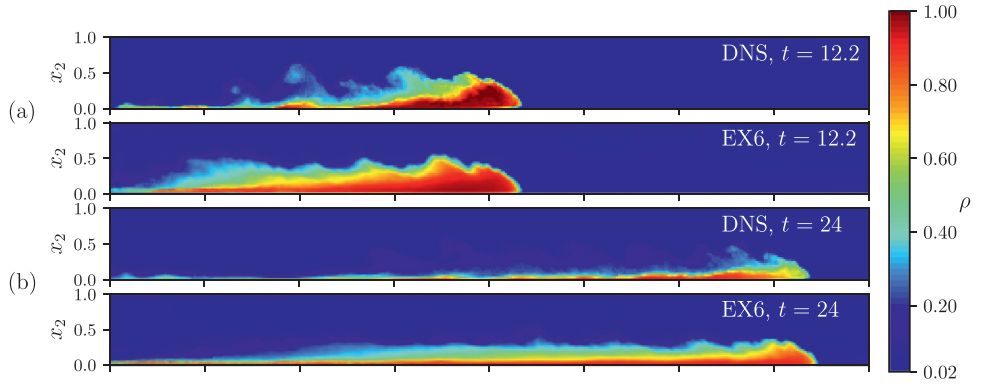

Fig. 6. Spanwise-averaged density field for the DNS (top) and EX6 (bottom) for (a) $t = 12.2$ and (b) $t = 24$.

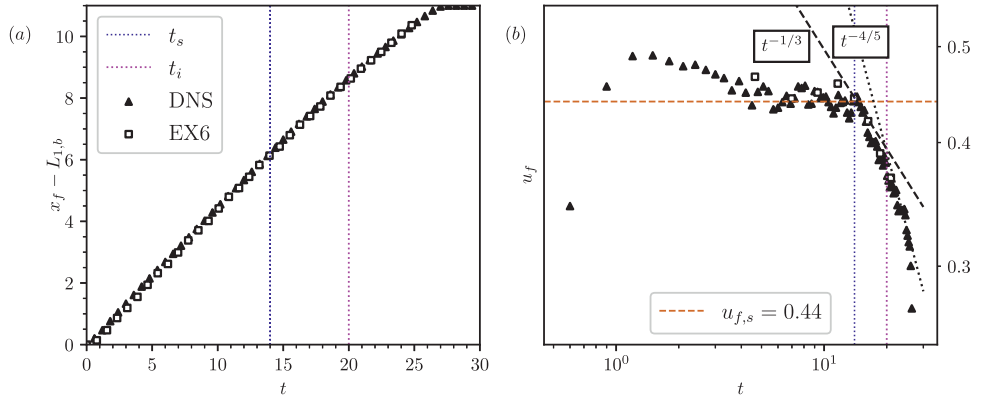

Fig. 7. Temporal evolution of the front position (a) and front velocity (b) for the DNS and EX6. t_s corresponds to the end of the slumping phase and t_i to the end of the inertial phase.

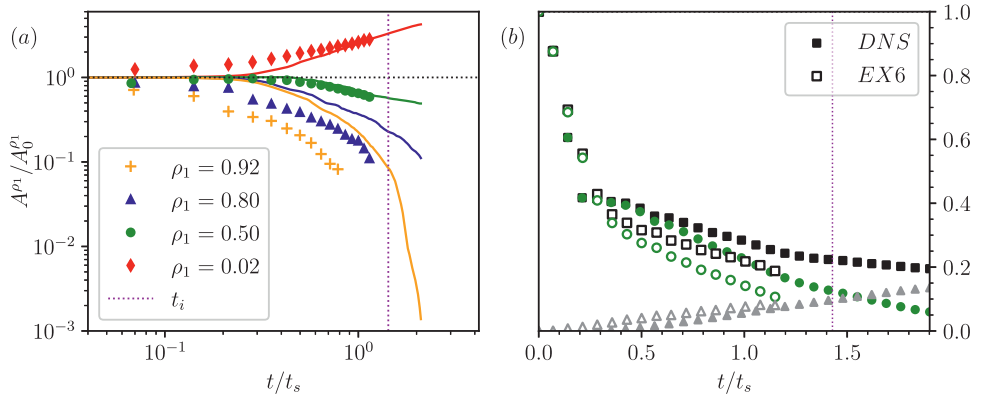

Fig. 8. (a) Temporal evolution of $A^{\rho_1}(t)/A^{\rho_1}_{t=0}$ for different density thresholds. The solid lines correspond to the DNS, and the symbols to EX6. (b) Temporal evolution of the normalised energy. Here, the black square symbols correspond to the total potential energy $\mathcal{P}(t)$, the grey triangle symbols to the background potential energy $\mathcal{P}_b$ and the green circle symbols to the difference between the two. Data are normalised so that the minimum total potential energy is zero and the maximum total potential energy is 1. Time is scaled by t_s.. (For interpretation of the references to colour in this figure legend, the reader is referred to the web version of this article.)

measurements of mixing cannot rely on density threshold methods alone and must include an integral method, such as rearranged potential energy, to characterise the evolution of a continuous density field, in agreement with the findings of [33].

Fig. 8 b compares the time evolution of total, available and background energy for EX6 and the DNS. For this figure, each term is normalised so that the minimum total potential energy is zero and the maximum total potential energy is 1, while the time is scaled by the time required to reach the slumping distance. The DNS is able to capture the initial strong decay of available energy, up to $t/t_s \approx 0.3$, followed by a more moderate decay afterwards where the DNS over-predicts the available energy by comparison to the experiment, with a 15% to 25% difference. It suggests that the noisy removal of the gate in the experiment might have consumed a fair amount of available energy, hence the lowest values reported in the experiment after $t/t_s \approx 0.5$. Further investigations would be needed to confirm this point. More details about the behaviour of $\mathcal{P}_a$ and $\mathcal{P}_b$ is provided in the next section.

Overall, the DNS is able to capture accurately the main features of the gravity current, with a good agreement with the experiment EX6 of [33], except for the temporal evolution of low and high density thresholds. In the following, the DNS will be used as a reference to evaluate the performance of the LES models.

4. LES results

The present study aims to assess the ability of LES to reproduce the main features of a high-Reynolds number gravity current in a channelised lock-exchange set-up, at a fraction of the cost of the DNS. In this section, several LES are performed, with the standard Smagorinsky model (SSM), with the dynamic Smagorinsky model (DSM) and with the SVV model based on high-order finite-difference schemes. The spatial resolution of the LES has been chosen to be as small as possible while making sure that the LES are stable without any numerical artefact (no limiters to constrain the density field to values between 0 and 1 or filtering procedures to remove numerical oscillations are used in the present LES). The spatial resolution for the LES is $n_1 \times n_2 \times n_3 = 577 \times 201 \times 24$ mesh nodes, a reduction of more than a factor 7, 3.8 and 10 in the streamwise, vertical and spanwise directions, respectively, by comparison to the DNS data. Expressed in wall viscous units, it corresponds to a maximal resolution of $\Delta^+_{x_{1\max}} \approx 10/15$, $\Delta^+_{x_{2\max}} \approx 2$ and $\Delta^+_{x_{3\max}} \approx 10/15$. Those values have been obtained by calculating the maximum value of the spanwise-averaged wall shear velocity at each time step. They are in line with the recommendations of [85] who suggested that the first off-wall mesh node should lie in the viscous sublayer of the current at the bottom wall. The streamwise and spanwise values are much smaller than the values reported in [77] ($\Delta^+_{x_{1\max}} \approx 50$, $\Delta^+_{x_{2\max}} \approx 1$ and $\Delta^+_{x_{3\max}} \approx 20$). For consistency, the same small time step is used for the DNS and the LES so that temporal discretisation errors are negligible. It means that the present LES are about 275 times cheaper than the DNS. The first important result is that the SSM LES and DSM LES are 1.8 and 2.5 times more expensive than the SVV model, respectively, as the latter does not require any explicit terms in the Navier-Stokes equations nor filtering.

As described in Section 2.4, the SVV model relies on a physical scaling of the numerical dissipation introduced when evaluating the viscous term of the Navier-Stokes equations. To estimate the physical scaling of ν_0/ν, the strategy proposed by Dairay et al. [20] has been used. It is based on a Pao-like spectral closure established on physical arguments to scale the numerical viscosity. With the current mesh resolution, the theoretical prediction of the scaling is $\nu_0/\nu = 60$ (simulation SVV60). It should be noted that this estimate was designed for homogeneous isotropic turbulence; hence the theoretical prediction of this scaling might not be accurate for gravity currents (stratified transitional flows in the presence of a wall). A sensitivity analysis is presented in Appendix A. It can be seen that for the range of ν_0/ν investigated, the quality of the results does not change much when compared to the DNS data of reference.

4.1. Instantaneous data

In Fig. 9 iso-contours of $Q - criterion = 50$ and of $\rho = 0.01$ are presented for $t = 15$, when the current has reached a fully turbulent state. As expected, a wider range of turbulent scales can be observed for the DNS, with very fine vortices at the head of the current and at the interface between the heavy fluid and the lighter fluid. The LES do not produce obvious spurious oscillations, except close to the heavy/light fluid interface for the explicit mod-

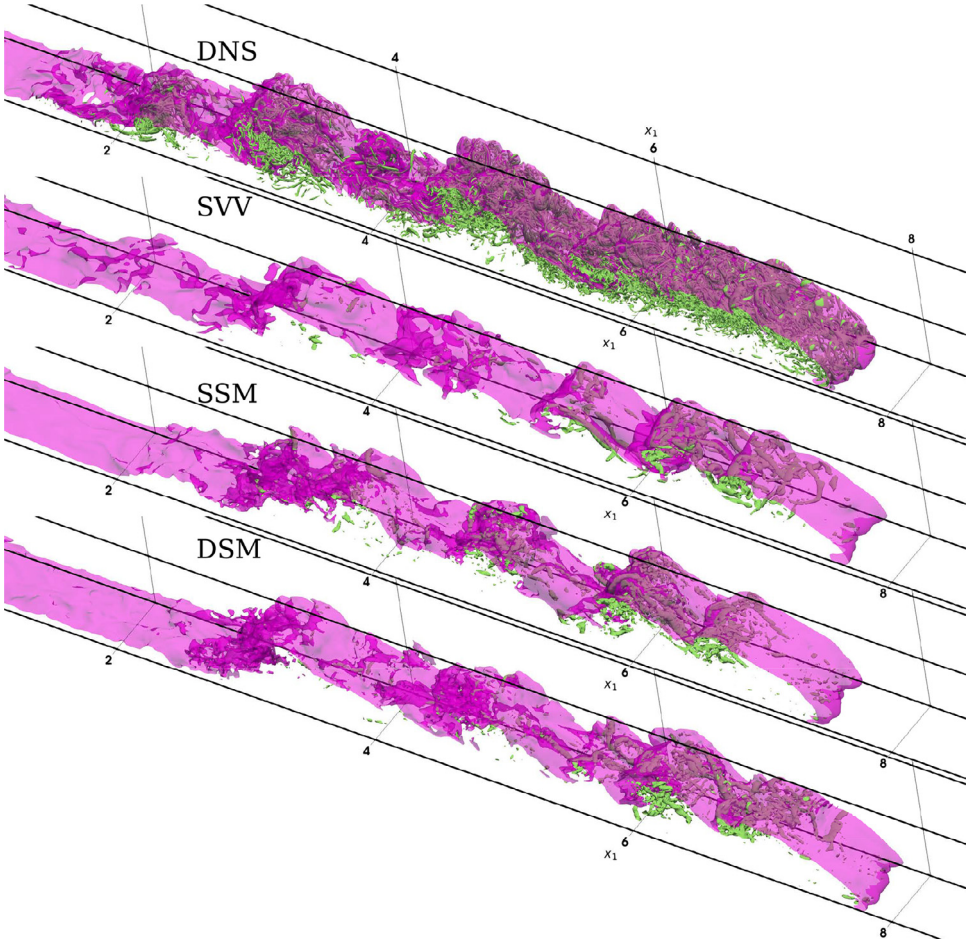

Fig. 9. Isocontours of the Q-criterion ($Q = 50$ in green) and the density field $\rho = 0.1$ (pink) at $t = 15$. From top to bottom: DNS, SVV60, SSM and DSM. (For interpretation of the references to colour in this figure legend, the reader is referred to the web version of this article.)

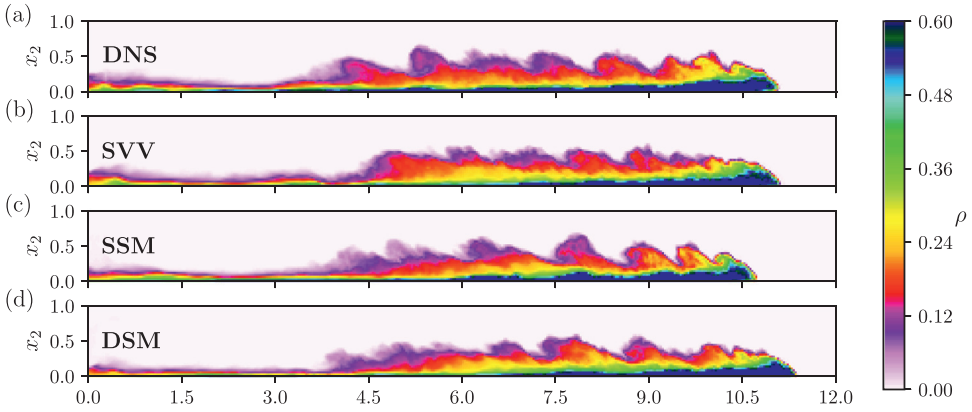

Fig. 10. 2D visualisations of the spanwise averaged density field at $t = 24$: (a) DNS, (b) SVV60, (c) SSM, (d) DSM.

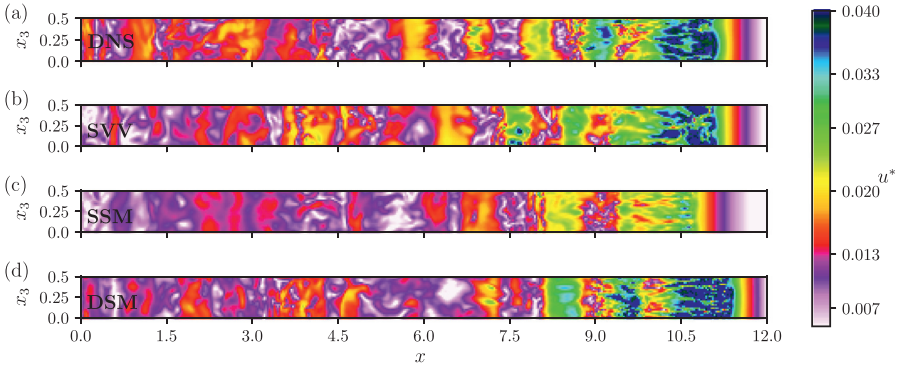

Fig. 11. 2D friction velocity maps at $t = 24$: (a) DNS, (b) SVV60, (c) SSM, (d) DSM.

els (SSM and DSM) for $x_1 \approx 3, 4.5$ and $x_1 \approx 6.5$. At these locations, the streamwise-orientated elongated structures are not as well defined as for the SVV model due to the presence of small non-physical oscillations. The head of the current for the DSM is further ahead than the one in the DNS. For the two explicit LES, the tail of the current (where vortical structures are no longer observable) seems to be further downstream from the inlet than in the SVV LES and DNS.

The spanwise-averaged density field at $t = 24$ is presented in Fig. 10. It can be seen that the current for the DSM is indeed travelling faster than the current in the DNS while the current in the SSM is travelling slower than the current in the DNS. The LES seems to be able to reproduce properly the main features of the current, in particular the characteristic Kelvin-Helmholtz vortices generated at the head of the current and convected upstream at the heavy/light fluid interface. Furthermore, there seems to be a good agreement between the LES and DNS regarding the different colour thresholds representing different density values.

The friction velocity and associated wall shear stress can be used in a simulation to estimate the critical shear stress level beyond which incipient motion can occur. Such an approach, first introduced by Shields [97], is based on a similarity method for sediment process, yielding to the Shields diagram. It remains the most widely used strategy to estimate the potential for incipient motion of particles and has been applied in several experimental and numerical works [32,47,71,76,103,105,113]. It should be noted however that incipient motion is very often neglected as the configurations studied in laboratory experiments and via high-fidelity simulations cannot replicate the erosion process observed in real-life currents due to the limitation in the Reynolds number. The correct reproduction of the friction velocity is nevertheless an interesting (and challenging to reproduce) quantity of interest to assess the quality of LES models. 2D maps of the friction velocity u^* are presented in Fig. 11 for $t = 24$. The friction velocity is defined as

$$u^* = \sqrt{\tau_w} \quad \text{with} \quad \tau_w = \frac{1}{Re}\sqrt{\left(\frac{\partial u_1}{\partial x_2}\right)^2 + \left(\frac{\partial u_3}{\partial x_2}\right)^2}\Bigg|_{x_2=0}. \tag{35}$$

According to Fig. 11, the best agreement for the friction velocity is obtained for the SVV model, followed by the DSM. The SSM is not able to capture the high values of the friction velocity at the head of the current. It can be connected to a high-level of numerical dissipation at the bottom of the channel. Non-uniformities are observed at the head of the current, a signature of the well-known lobe-and-cleft structures, characterised with intense friction velocities with a streaky pattern (dark blue in the figure). These imprints cannot be captured properly by the SSM.

The formation, merging and meandering of the lobe-and-cleft structures at the front of the current can be seen in Fig. 12 with iso-lines of the bottom wall density field ($\rho = 0.01$). These structures arise from an instability produced by the ambient fluid, which is overrun by the heavy fluid, and it is one of the main features of gravity currents. As expected, the DNS generates a wider range of lobe-and-cleft structures, with more merging and meandering by comparison to the LES. It seems that less splitting and merging events are present for the explicit LES models as for the SVV model. It is consistent with the overly dissipative behaviour reported in Fig. 11 for the friction velocity.

4.2. Averaged data

The temporal evolution of the front position and front velocity for the LES is presented in Fig. 13. As already hinted with the instantaneous visualisation of the current in the previous subsection, it can be seen that the SSM and DSM are not able to ac-

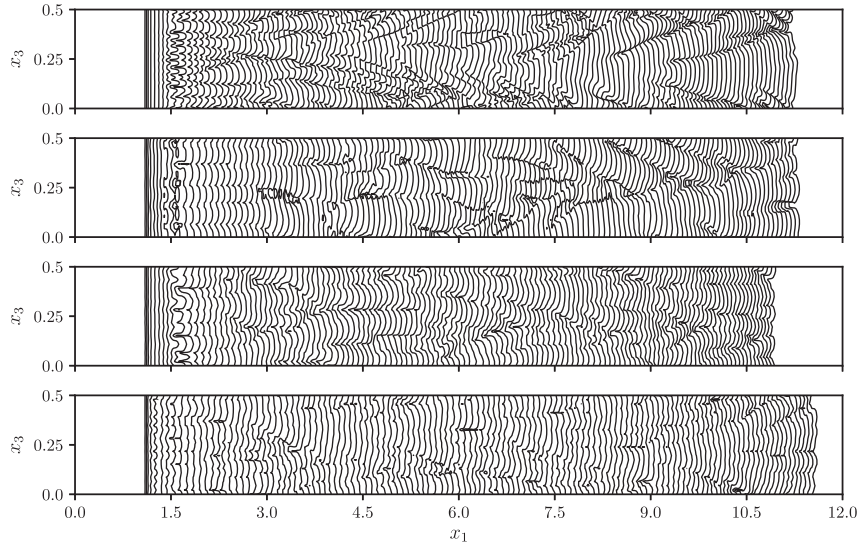

Fig. 12. Temporal evolution of the isolines of the bottom wall density field ($\rho = 0.01$) for (a) DNS, (b) SVV60, (c) SSM, (d) DSM.

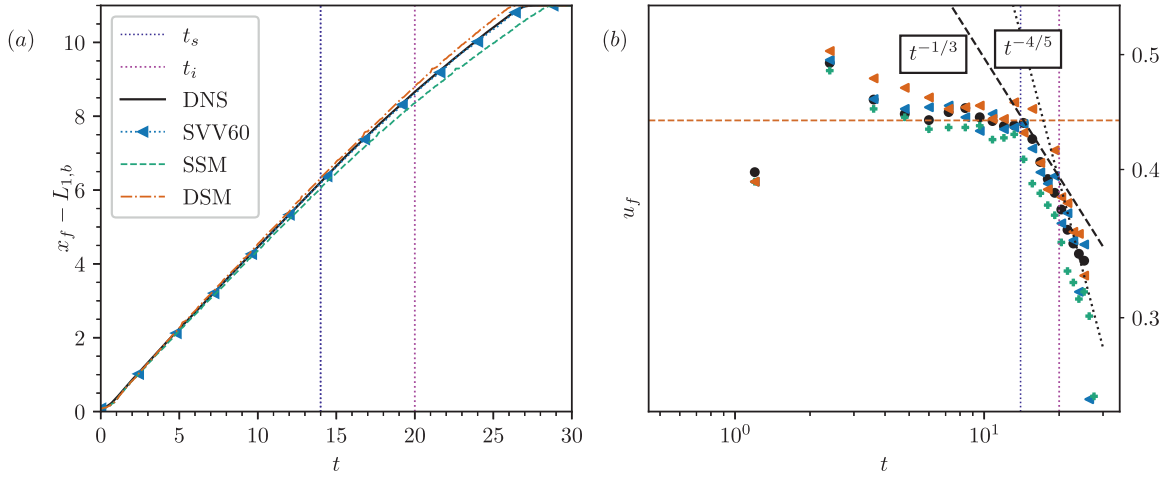

Fig. 13. Temporal evolution of the front position (a) and front velocity (b) for the various LES.

curately capture the correct location of the front position after the slumping phase. The SVV model is able to capture perfectly the location of the front. The SSM is underestimating the front location, with a deviation from the DNS data starting at the end of the slumping phase. The DSM is slightly overestimating the front location after the slumping phase, in line with the results of [78]. Note that an excellent agreement between LES and experiments for the front location was reported in [80] but only for very low Reynolds numbers. Despite this minor discrepancy for the SSM, explicit LES models are more or less able to capture the power-law decays when the current is slowing down, after the slumping phase (the front velocity for the DSM is just slightly higher than the DNS one and it is lower for the SSM).

Fig. 14 a shows the temporal evolution of the dilution of the heavy fluid into the ambient fluid by using the same thresholds used in the experiment of [33], see Fig. 8. It can be seen that all the LES are able to match the DNS data of reference, especially for high thresholds. For the lowest threshold of 0.02, it seems that the DSM is in slightly better agreement with the DNS, while the dilution for the SVV model and SSM is marginally faster for $\rho_1 = 0.02$.

Fig. 14 b shows the temporal evolution of the total mass expressed as

$$m_s(t) = \int_V \rho(x_1, x_2, x_3, t)\mathrm{d}V. \tag{36}$$

It can be seen that all the LES models are capable of conserving the total mass with high accuracy, within less than 0.05%. It suggests that the LES models do not introduce large spurious oscillations to the current. For the explicit LES models, a small amount of mass is numerically created soon after the release of the heavy fluid, up to $t = 10$ for the DSM and up to $t = 20$ for the SSM. For the DSM, mass is removed from the current from $t = 10$ onward while the mass is more or less conserved for the SSM and the SVV model. It suggests that the DSM might have an under-dissipative behaviour at the start of the simulation (with a fast-moving current) and an over-dissipative behaviour when the current is fully established.

The total energy budget is presented in Fig. 15a while the temporal evolution of the energy transfer mechanisms (vertical buoyancy flux and mixing) is presented in Fig. 15b. In order to account for the numerical dissipation, the calculation of the internal energy needs to be modified as follow

$$\mathcal{I}(t) = \int_0^t [\epsilon(t) - \Phi(t)]\mathrm{d}t + \mathcal{I}_{LES}. \tag{37}$$

Following a strategy introduced in [101], $\mathcal{I}_{LES}$, which accounts for contribution of the numerical dissipation to the dissipation rate, can be evaluated as a residual

$$\mathcal{I}_{LES}(t) = \mathcal{T}(t = 0) - \mathcal{T}(t). \tag{38}$$

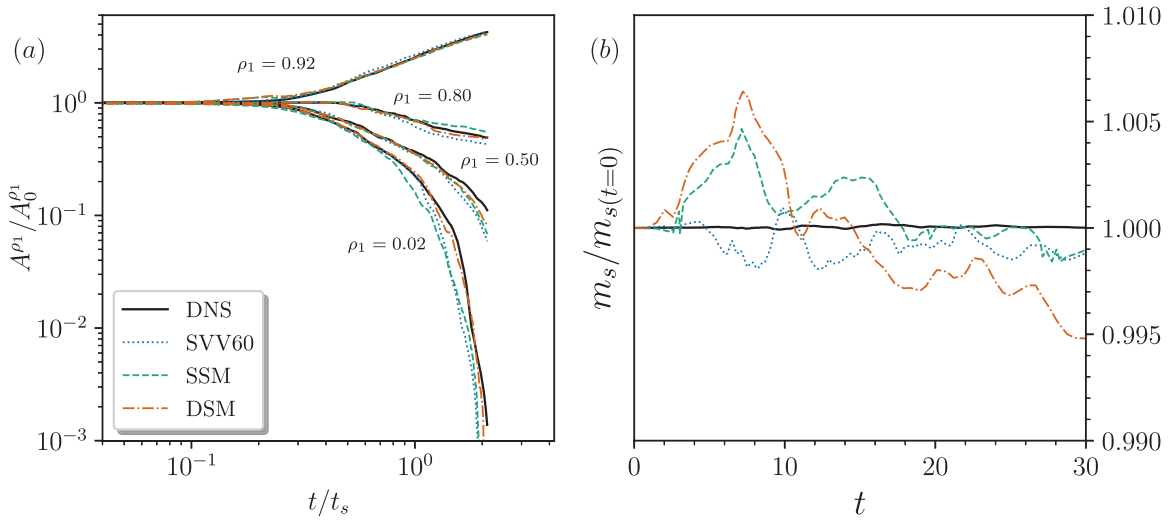

Fig. 14. Temporal evolution of the dilution for different thresholds for the density field (a) and the global mass (b) for the DNS and the LES.

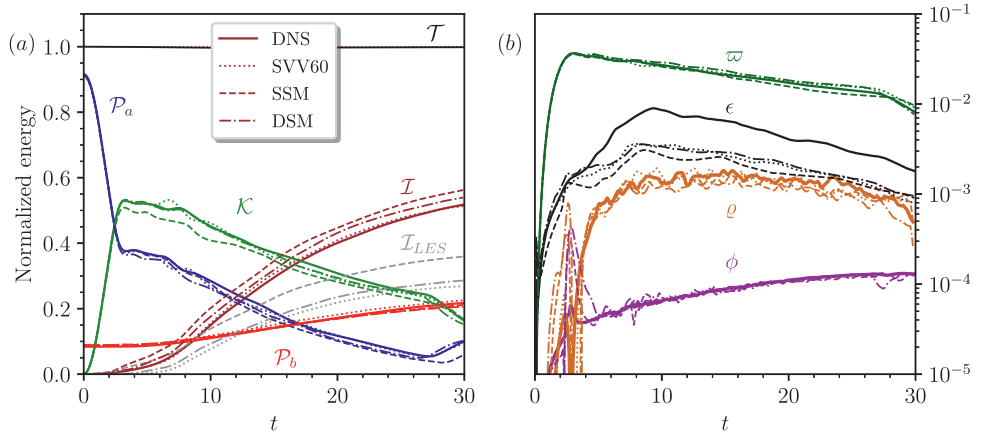

Fig. 15. Temporal evolution of the energy budget normalised by the total initial energy (a) and the energy transfer mechanisms (b). The solid lines corresponds to the DNS, the dotted lined to the SVV60, the dashed lines to the SSM and the dash-dotted lines to the DSM.

The main assumption of this approach is that the energy is perfectly conservation for the LES. In the DNS, $\mathcal{I}_{LES}(t)$ is of course equal to zero (which is the case in our DNS).

It can be seen in Fig. 15 that at the very early stage of the simulations, there is a swift drop of available potential energy $\mathcal{P}_a$, up to $t \approx 4$, associated with a rapid increase of total kinetic energy $\mathcal{K}$. This rapid increase is produced by a strong vertical buoyancy flux ϖ as shown in Fig. 15b. Over 50% of the available potential energy is transferred into total kinetic energy. It corresponds to the important amount of energy used by the current to establish itself following the removal of the gate. Very little irreversible dyapicnal mixing ϱ, defined as an irreversible energy transfer mechanism acting towards smoothing the density field, is occurring at the start of the simulations, which is consistent with a quasi-steady background energy (only diabatic mixing can produce changes in the background state, see [112]).

After the peak of total kinetic energy, the available potential energy and total kinetic energy exhibit a steady decay, associated with an increase in internal energy and background potential energy associated with a sustained mixing activity (with ϱ nearly constant). The vertical buoyancy flux ϖ and viscous dissipation ε are steadily decreasing after the total kinetic energy peak, while the density diffusion Φ is increasing and the irreversible dyapicnal mixing ϱ is more or less steady. The small increase in available potential energy and the sudden decrease in total kinetic energy at the end of the simulations are linked to the current reaching the end of the computational domain for $t \approx 27$. By the end of the simulation, the available potential energy is as low as 10% of its initial value. Most of the available potential energy has been converted as internal energy (more than 50%). The main mechanism of transfer of energy is the vertical buoyancy flux, which is more or less two orders of magnitude larger than the density diffusion, one order of magnitude larger than the irreversible dyapicnal mixing, and much larger than the viscous dissipation.

Overall, all the LES are able to reproduce the energy budget and the evolution of the transfer mechanisms obtained in the DNS, with only minor differences such as an over-estimation of the internal energy for the SSM model of about $10-15\%$, associated with a slight under-prediction of the total kinetic energy of about $5-10\%$. It is a confirmation that the SSM is possibly too dissipative ($\mathcal{I}_{LES}$ is much larger for the SSM than for the DSM), especially in high shear/low turbulence regions. The DSM and SVV model have a consistent behaviour, with a similar amount of numerical dissipation added to the current and only a marginal overestimation of the internal energy for the DSM with respect to the DNS. As expected, the viscous dissipation ε is under-predicted in the LES by comparison to the DNS as ε is computed with first order derivatives for which there is no added numerical dissipation. ε is slightly more under-predicted for the SSM than for the DSM and SVV model. The LES seem to be able to capture accurately the

available and background potential energy from the DNS. A similar observation was already reported in [75] where the background potential energy was used to assess the performance of 6 different LES models for lock-exchange gravity currents. A small peak of insignificant importance for the dynamic of the current (two order of magnitude small than the vertical buoyancy flux ϖ) can be observed in for ϱ and Φ at $t \approx 3$. This peak is over-estimated in the LES by comparison to the DNS, especially for the DSM, however with virtually no impact on the temporal evolution of the energy transfer mechanisms after the peak (confirmed by the good agreement with the DNS data).

5. Conclusions

In this numerical study, high-fidelity simulations of a gravity current in the lock-exchange set-up have been performed and compared with experimental data. The potential of using a high-order finite-difference SVV approach in the context of LES was investigated with a detailed comparison with more conventional LES based on explicit SGS model and with a resolved DNS. The DNS was performed with more than 800 million mesh nodes and, it is to the best of our knowledge, a DNS of gravity currents in a lock-exchange set-up at the highest Reynolds number. The LES were performed with only less than 0.4% of the total number of mesh nodes of the DNS. An original energy framework was introduced to better understand the main features of the gravity currents.

One of the main conclusions of this study is that all LES models perform well at reproducing the main features of the gravity currents, however, the presented SVV model performs slightly better , in particular close to the bottom of the channel. It should be noted that the SVV model does not require any filtering nor the computation of extra terms in the Navier-Stokes equations, making it very competitive in terms of computational cost (the SSM and DSM are 1.8 and 2.5 times more expensive than the SVV model, respectively). Therefore, we may argue that the SVV model is up-and-coming for future high-fidelity simulations of gravity currents at much higher Reynolds numbers, with the potential to reach real-life parameters.

Our next study will focus on high-fidelity simulations of high Reynolds numbers Boussinesq gravity currents, thanks to the flow solver `QuasIncompact3D`, part of the `Xcompact3d` framework. This solver is based on the compressible Navier-Stokes equations in the low Mach number limit, allowing simulations of gravity currents with densities ratio of up to 10 between the heavy release and the ambient fluid [4]. High Reynolds numbers non-Boussinesq gravity currents in a basin set-up (where the current can freely evolve in the spanwise and streamwise directions, see [34]) will also be investigated.

It could also be of interest to investigate the potential of the present SVV model for turbulent flows where the mixing aspect is dominant, such as turbulent flows induced by Rayleigh-Taylor instabilities [116–118]. A two-phase flow solver based on the Allen-Cahn phase-field approach is currently under development within the `Xcompact3D` framework, as an extension of the existing `QuasIncompact3D` flow solver. This will allow us to study turbulent mixing induced by hydrodynamic instabilities such as the Rayleigh-Taylor, Richtmyer-Meshkov, and Kelvin-Helmholtz instabilities with potential applications in astrophysics, geophysics, and other engineering flows of both scientific interest and practical significance.

Declaration of Competing Interest

The authors declare that they have no known competing financial interests or personal relationships that could have appeared to influence the work reported in this paper.

CRediT authorship contribution statement

Ricardo A.S. Frantz: Conceptualization, Methodology, Software, Formal analysis. **Georgios Deskos:** Conceptualization, Methodology, Writing - review & editing. **Sylvain Laizet:** Writing - original draft, Writing - review & editing, Project administration. **Jorge H. Silvestrini:** Supervision, Writing - review & editing, Funding acquisition.

Acknowledgments

The authors acknowledge the National Laboratory for Scientific Computing (LNCC/MCTI, Brazil) for providing HPC resources of the SDumont supercomputer and EPSRC for access to the UK Supercomputing facility ARCHER via the UK Turbulence Consortium (EP/R029326/1). This study was funded by Petrobras and in part by the Coordenação de Aperfeiçoamento de Pessoal de Nível Superior - Brasil (CAPES) - Finance Code 001. The authors gratefully acknowledge Bruno A. Farenzena for his helpful insights for the energy budget analysis.

Appendix A. Sensitivity study for the SVV model

To investigate the sensitivity of ν_0/ν for the present lock-exchange set-up, five extra LES have been performed with ν_0/ν ranging from 15 to 90, with increment of 15 (simulations SVV15 to SVV90). Fig. A.16 shows spanwise-averaged visualisations of the density field at $t = 24$ for SVV45, SVV60 and SVV75. Overall, an excellent agreement with the DNS data of reference can be seen with very little difference when the numerical dissipation is changed. No spurious oscillations can be observed suggesting that enough numerical dissipation is added at small scales, even for SVV45. It should be noted that no numerical artefact is applied to the density field (no filtering nor limiters).

The front location and front velocity for the various SVV simulations are in excellent agreement with the DNS data of reference, as seen in Fig. A.17. Actually, all the SVV simulations are in better agreement with the DNS data than the explicit LES models. It is another evidence that the SVV model is not sensitive to ν_0/ν, as long as enough numerical dissipation is added to the flow.

Fig. A.18 a compares the temporal evolution of the dilution of the current for four thresholds, in a similar fashion to Fig. 14a. Once again, it can be seen that changing ν_0/ν does not affect the dilution of the heavy fluid in the ambient fluid. All the SVV models are in excellent agreement with the DNS data of reference, except maybe for the lowest threshold $\rho_1 = 0.02$ for which all the SVV models are marginally under-predicting the DNS data, with a slightly faster decay rate. The same observation can be drawn for the global mass which is perfectly conserved within 0.5%. It is, however clear that SVV15 is the simulation with the less accurate results. For the range of numerical dissipation considered here, the gravity current shows low sensitivity to the choice of ν_0/ν. The small discrepancies in Fig. A.18 can be attributed to discretisation errors.

Overall, the method proposed by Dairay et al. [20] to estimate the physical scaling of ν_0/ν seems to be perfectly capable of providing an adequate value numerical dissipation for the SVV model, even if it is designed for homogeneous isotropic turbulence. Another important observation is that adding too much numerical dissipation does not seem to affect the quality of the solution. It will however affect the stability of the simulation. The use of high values for ν_0/ν would require very small time steps because of the stability limit $\nu\Delta t/\Delta x^2 < \sigma_r/(\nu_0/\nu)\pi^2$ (with for instance $\sigma_r = 2.5$ for a third-order Runge-Kutta scheme, see [55]).

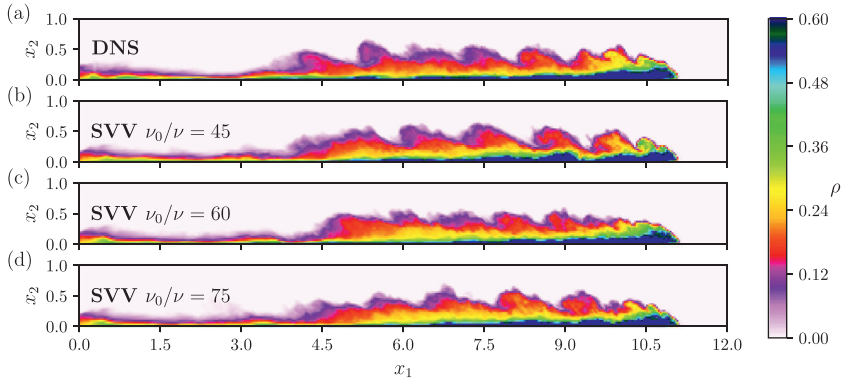

Fig. A.16. 2D visualisations of the spanwise averaged density field at $t = 24$ for the DNS and SVV45, SVV60 and SVV75.

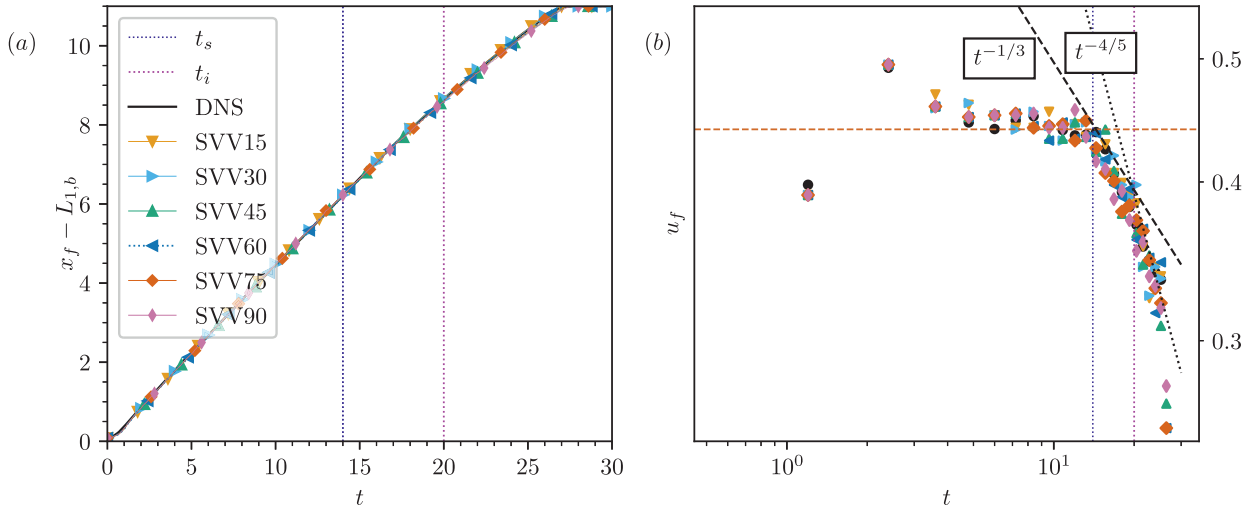

Fig. A.17. Temporal evolution of the front position (a) and front velocity (b) for the DNS and the various LES based on the SVV approach.

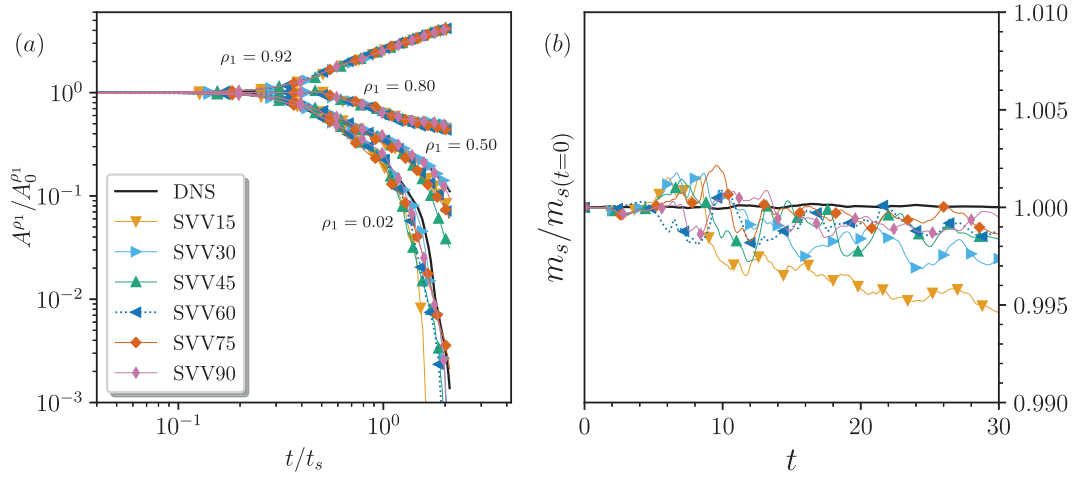

Fig. A.18. Temporal evolution of the dilution for different thresholds for the density field (a) and of the global mass (b) for the DNS and the various LES based on the SVV approach.

References

[1] Allen J. Principles of physical sedimentology. Springer Science & Business Media; 2012.

[2] Armenio V, Sarkar S. An investigation of stably stratified turbulent channel flow using large-eddy simulation. J Fluid Mech 2002;459:1–42.

[3] Bartholomew P, Deskos G, Frantz RA, Schuch FN, Lamballais E, Laizet S. Xcompact3D: an open-source framework for solving turbulence problems on a cartesian mesh. SoftwareX 2020;12:100550.

[4] Bartholomew P, Laizet S. A new highly scalable, high-order accurate framework for variable-density flows: application to non-Boussinesq gravity currents. Comput Phys Commun 2019;242:83–94.

[5] Bonnecaze R, Huppert H, Lister J. Particle-driven gravity currents. J Fluid Mech 1993;250:339–69.

[6] Bonometti T, Balachandar S. Effect of schmidt number on the structure and propagation of density currents. Theor Comput Fluid Dyn 2008;22(5):341.

[7] Boris J, Grinstein F, Oran E, Kolbe R. New insights into large eddy simulation. Fluid Dyn Res 1992;10(4–6):199–228.

[8] Britter R, Linden P. The motion of the front of a gravity current travelling down an incline. J Fluid Mech 1980;99(3):531–43.

[9] Britter R, Simpson J. Experiments on the dynamics of a gravity current head. J Fluid Mech 1978;88:223–40.
[10] Cantero M, Balachandar S, Garcia M. High-resolution simulations of cylindrical density currents. J Fluid Mech 2007;590:437–69.
[11] Cantero M, Lee J, Balachandar S, Garcia M. On the front velocity of gravity currents. J Fluid Mech 2007;586:1–39.
[12] Cantero MI, Balachandar S, García MH, Bock D. Turbulent structures in planar gravity currents and their influence on the flow dynamics. J Geophys Res Oceans 2008;113(C8).
[13] Canuto C, Hussaini MY, Quarteroni A, Thomas A Jr, et al. Spectral methods in fluid dynamics. Springer Science & Business Media; 2012.
[14] Cerutti S, Meneveau C, Knio OM. Spectral and hyper eddy viscosity in high-Reynolds-number turbulence. J Fluid Mech 2000;421:307–38.
[15] Chawdhary S, Khosronejad A, Christodoulou G, Sotiropoulos F. Large eddy simulation of density current on sloping beds. Int J Heat Mass Transf 2018;120:1374–85.
[16] Chollet J-P, Lesieur M. Parameterization of small scales of three-dimensional isotropic turbulence utilizing spectral closures. J Atmos Sci 1981;38(12):2747–57.
[17] Chow FK, Moin P. A further study of numerical errors in large-eddy simulations. J Comput Phys 2003;184(2):366–80.
[18] Constantinescu G. LES of lock-exchange compositional gravity currents: a brief review of some recent results. Environ Fluid Mech 2014;14(2):295–317.
[19] Dairay T, Fortuné V, Lamballais E, Brizzi L. LES of a turbulent jet impinging on a heated wall using high-order numerical schemes. Int J Heat Fluid Flow 2014;50:177–87.
[20] Dairay T, Lamballais E, Laizet S, Vassilicos JC. Numerical dissipation vs. subgrid-scale modelling for large eddy simulation. J Comput Phys 2017;337:252–74.
[21] De Falco M, Adduce C, Negretti M, Hopfinger E. On the dynamics of quasi-steady gravity currents flowing up a slope. Adv Water Resour 2021;147:103791.
[22] De Falco M, Ottolenghi L, Adduce C. Dynamics of gravity currents flowing up a slope and implications for entrainment. J Hydraul Eng 2020;146(4):04020011.
[23] de Rooij F, Dalziel S. Time- and space-resolved measurements of deposition under turbidity currents. Spec Publs Int Ass Sediment 2001;31:207–15.
[24] Deskos G, Laizet S, Palacios R. WInc3D: a novel framework for turbulence-resolving simulations of wind farm wake interactions. Wind Energy 2020;23(3):779–94.
[25] Deskos G, Laizet S, Piggott MD. Turbulence-resolving simulations of wind turbine wakes. Renew Energy 2019;134:989–1002.
[26] Ellison TH, Turner JS. Turbulent entrainment in stratified flows. J Fluid Mech 1959;6(3):423–48.
[27] Emami S-M-K, Mousavi S-F, Hosseini K, Fouladfar H, Mohammadian M. Comparison of different turbulence models in predicting cohesive fluid mud gravity current propagation. Int J Sediment Res 2020.
[28] Espath LFR, Pinto LC, Laizet S, Silvestrini JH. Two- and three-dimensional direct numerical simulation of particle-laden gravity currents. Comput Geosci 2014;63:9–16.
[29] Espath LFR, Pinto LC, Laizet S, Silvestrini JH. High-fidelity simulations of the lobe-and-cleft structures and the deposition map in particle-driven gravity currents. Phys Fluids 2015;27(5):056604.
[30] Falkovich G. Bottleneck phenomenon in developed turbulence. Phys Fluids 1994;6(4):1411–14.
[31] la Forgia G, Tokyay T, Adduce C, Constantinescu G. Numerical investigation of breaking internal solitary waves. Phys Rev Fluids 2018;3(10):104801.
[32] la Forgia G, Tokyay T, Adduce C, Constantinescu G. Bed shear stress and sediment entrainment potential for breaking of internal solitary waves. Adv Water Resour 2020;135:103475.
[33] Fragoso AT, Patterson MD, Wettlaufer JS. Mixing in gravity currents. J Fluid Mech 2013;734:R2.
[34] Francisco EP, Espath LFR, Laizet S, Silvestrini JH. Reynolds number and settling velocity influence for finite-release particle-laden gravity currents in a basin. Comput Geosci 2018;110:1–9.
[35] Germano M, Piomelli U, Moin P, Cabot WH. A dynamic subgrid-scale eddy viscosity model. Phys Fluids A Fluid Dyn 1991;3(7):1760–5.
[36] Ghosal S. An analysis of numerical errors in large-eddy simulations of turbulence. J Comput Phys 1996;125(1):187–206.
[37] Gladstone C, Phillips JC, Sparks RSJ. Experimentation on bidisperse, constant-volume gravity curents: propagation and sediment deposition.. Sedimentology 1998;46:833–43.
[38] Gonzalez-Juez E, Meiburg E, Tokyay T, Constantinescu G. Gravity current flow past a circular cylinder: forces, wall shear stresses and implications for scour. J Fluid Mech 2010;649:69–102.
[39] Grinstein FF, Fureby C. From canonical to complex flows: recent progress on monotonically integrated LES. Comput Sci Eng 2004;6(2):36–49.
[40] Grundy R, Rottmant JW. Self-similar solutions of the shallow-water equations representing gravity currents with variable inflow. J Fluid Mech 1986;169:337–51.
[41] Härtel C, Kleiser L, Michaud M, Stein C. A direct numerical simulation approach to the study of intrusion fronts. J Eng Math 1997;32(2–3):103–20.
[42] Härtel C, Meiburg E, Necker F. Analysis and direct numerical simulation of the flow at a gravity-current head. Part 1. Flow topology and front speed for slip and no-slip boundaries. J Fluid Mech 2000;418:189–212.
[43] Haugen NEL, Brandenburg A. Inertial range scaling in numerical turbulence with hyperviscosity. Phys Rev E 2004;70:026405.
[44] Huppert H, Simpson J. The slumping of gravity currents. J Fluid Mech 1980;99(04):785–99.
[45] Inghilesi R, Adduce C, Lombardi V, Roman F, Armenio V. Axisymmetric three-dimensional gravity currents generated by lock exchange. J Fluid Mech 2018;851:507–44.
[46] Ioannou V, Laizet S. Numerical investigation of plasma-controlled turbulent jets for mixing enhancement. Int J Heat Fluid Flow 2018;70:193–205.
[47] Julien P. Erosion and sedimentation. Cambridge University Press; 2010.
[48] Karamanos G, Karniadakis GE. A spectral vanishing viscosity method for large-eddy simulations. J Comput Phys 2000;163(1):22–50.
[49] Kirby R, Karniadakis G. Coarse resolution turbulence simulations with spectral vanishing viscosity–large-eddy simulations (SVV-LES). ASME J Fluids Eng 2002;124(4).
[50] Kraichnan RH. Eddy viscosity in two and three dimensions. J Atmos Sci 1976;33(8):1521–36.
[51] Kravchenko A, Moin P. On the effect of numerical errors in large eddy simulations of turbulent flows. J Comput Phys 1997;131(2):310–22.
[52] Kyrousi F, Leonardi A, Roman F, Armenio V, Zanello F, Zordan J, et al. Large eddy simulations of sediment entrainment induced by a lock-exchange gravity current. Adv Water Resour 2018;114:102–18.
[53] Laizet S, Lamballais E. High-order compact schemes for incompressible flows: a simple and efficient method with the quasi-spectral accuracy. J Comp Phys 2009;228:5989–6015.
[54] Laizet S, Li N. Incompact3d: a powerfull tool to tackle turbulence problems with up to $O(10^5)$ computational cores. Int J Numer Methods Fluids 2011;67:1735–57.
[55] Lamballais E, Fortune V, Laizet S. Straightforward high-order numerical dissipation via the viscous term for direct and large eddy simulation. J Comp Phys 2011;230(9):3270–5.
[56] Lele SK. Compact finite difference schemes with spectral-like resolution. J Comp Phys 1992;103:16–42.
[57] Lesieur M, Metais O. New trends in large-eddy simulations of turbulence. Annu Rev Fluid Mech 1996;28(1):45–82.
[58] Lesieur M, Rogallo R. Large-eddy simulation of passive scalar diffusion in isotropic turbulence. Phys Fluids A Fluid Dyn 1989;1(4):718–22.
[59] Lilly DK. The representation of small-scale turbulence in numerical simulation experiments. In: IBM Scientific computing symposium on environmental sciences. Thomas J. Watson Research Center, Yorktown; 1966. p. 195–210.
[60] Lilly DK. A proposed modification of the Germano subgrid-scale closure method. Phys Fluids A Fluid Dyn 1992;4(3):633–5.
[61] Lorenz EN. Available potential energy and the maintenance of the general circulation. Tellus 1955;7(2):157–67.
[62] Lucchese LV, Monteiro LR, Schettini EBC, Silvestrini JH. Direct numerical simulations of turbidity currents with evolutive deposit method, considering topography updates during the simulation. Comput Geosci 2019;133:104306.
[63] Mahdinia M, Firoozabadi B, Farshchi M, Varnamkhasti AG, Afshin H. Large eddy simulation of lock-exchange flow in a curved channel. J Hydraul Eng 2011;138(1):57–70.
[64] Martin A, Negretti M, Ungarish M, Zemach T. Propagation of a continuously supplied gravity current head down bottom slopes. Phys Rev Fluids 2020;5(5):054801.
[65] Martin A, Negretti M-E, Hopfinger EJ. Development of gravity currents on slopes under different interfacial instability conditions. J Fluid Mech 2019;880:180–208.
[66] Meiburg E, Radhakrishnan S, Nasr-Azadani M. Modeling gravity and turbidity currents: computational approaches and challenges. Appl Mech Rev 2015;67(4).
[67] Meneveau C, Katz J. Scale-invariance and turbulence models for large-eddy simulation. Annu Rev Fluid Mech 2000;32(1):1–32.
[68] Meneveau C, Lund TS. The dynamic Smagorinsky model and scale-dependent coefficients in the viscous range of turbulence. Phys Fluids 1997;9(12):3932–4.
[69] Meneveau C, Lund TS, Cabot WH. A lagrangian dynamic subgrid-scale model of turbulence. J Fluid Mech 1996;319:353–85.
[70] Métais O, Lesieur M. Spectral large-eddy simulation of isotropic and stably stratified turbulence. J Fluid Mech 1992;239:157–94.
[71] Nasr-Azadani M, Meiburg E. Turbidity currents interacting with three-dimensional seafloor topography. J Fluid Mech 2014;745:409–43.
[72] Necker F, Hartel C, Kleiser L, Meiburg E. High-resolution simulations of particle-driven gravity currents. Int J of Multiphase Flow 2002;28:279–300.
[73] Necker F, Härtel C, Kleiser L, Meiburg E. Mixing and dissipation in particle–driven gravity currents. J Fluid Mech 2005;545:339–72.
[74] Nogueira HI, Adduce C, Alves E, Franca MJ. Dynamics of the head of gravity currents. Environ Fluid Mech 2014;14(2):519–40.
[75] Oezgoekmen TM, Iliescu T, Fischer PF. Large eddy simulation of stratified mixing in a three-dimensional lock-exchange system. Ocean Modell 2009;26(3–4):134–55.
[76] Ooi SK, Constantinescu G, Weber L. Numerical simulations of lock-exchange compositional gravity current. J Fluid Mech 2009;635:361–88.
[77] Ottolenghi L, Adduce C, Inghilesi R, Armenio V, Roman F. Entrainment and mixing in unsteady gravity currents. J Hydraul Res 2016;54(5):541–57.
[78] Ottolenghi L, Adduce C, Inghilesi R, Roman F, Armenio V. Mixing in lock-release gravity currents propagating up a slope. Phys Fluids 2016;28(5):056604.

[79] Ottolenghi L, Cenedese C, Adduce C. Entrainment in a dense current flowing down a rough sloping bottom in a rotating fluid. J Phys Oceanogr 2017;47(3):485–98.
[80] Ottolenghi L, Prestininzi P, Montessori A, Adduce C, La Rocca M. Lattice Boltzmann simulations of gravity currents. Eur J Mech-B/Fluids 2018;67:125–36.
[81] Özgökmen TM, Iliescu T, Fischer PF. Reynolds number dependence of mixing in a lock-exchange system from direct numerical and large eddy simulations. Ocean Modell 2009;30(2–3):190–206.
[82] Pasquetti R. Spectral vanishing viscosity method for LES: sensitivity to the SVV control parameters. J Turbul 2005;6:N12.
[83] Pasquetti R, Séverac E, Serre E, Bontoux P, Schäfer M. From stratified wakes to rotor–stator flows by an SVV–LES method. Theor Comput Fluid Dyn 2008;22:261–73.
[84] Patterson MD, Caulfield C, McElwaine J, Dalziel S. Time-dependent mixing in stratified Kelvin-Helmholtz billows: experimental observations. Geophys Res Lett 2006;33(15).
[85] Pelmard J, Norris S, Friedrich H. LES grid resolution requirements for the modelling of gravity currents. Comput Fluids 2018;174:256–70.
[86] Pelmard J, Norris S, Friedrich H. Statistical characterisation of turbulence for an unsteady gravity current. J Fluid Mech 2020;901.
[87] Pierce CD. Progress-variable approach for large-eddy simulation of turbulent combustion. Stanford University; 2001. Ph.D. thesis.
[88] Piper D, Cochonat P, Morrison M. The sequence of events around the epicentre of the 1929 grand banks earthquake: initiation of the debris flows and turbidity current inferred from side scan sonar subaqueous sediment density flows: depositional processes and deposit types. Sedimentology 1999;46(1):79–97.
[89] Pope S. Turbulent flows. Cambridge University Press; 2000.
[90] van Reeuwijk M, Krug D, Holzner M. Small-scale entrainment in inclined gravity currents. Environ Fluid Mech 2018;18(1):225–39.
[91] Roman F, Stipcich G, Armenio V, Inghilesi R, Corsini S. Large eddy simulation of mixing in coastal areas. Int J Heat Fluid Flow 2010;31(3):327–41.
[92] Rottman JW, Simpson JE. Gravity currents produced by instantaneous releases of a heavy fluid in a rectangular channel. J Fluid Mech 1983;135:95–110.
[93] Sagaut P. Large eddy simulation for incompressible flows: an introduction. Springer Science & Business Media; 2006.
[94] Schuch FN, Pinto LC, Silvestrini JH, Laizet S. Three-dimensional turbulence-resolving simulations of the plunge phenomenon in a tilted channel. J Geophys Res Oceans 2018;123(7):4820–32.
[95] Sher D, Woods AW. Gravity currents: entrainment, stratification and self-similarity. J Fluid Mech 2015;784:130–62.
[96] Sher D, Woods AW. Mixing in continuous gravity currents. J Fluid Mech 2017;818.
[97] Shields A. Anwendung der ahnlichkeitsmechanik und der turbulenz-forschung auf die geschiebebewegung. A Mitteilungen der (Preussischen) Versuchsanstalt; 1936. Ph.D. thesis.
[98] Shin JO, Dalziel SB, Linden PF. Gravity currents produced by lock exchange. J Fluid Mech 2004;521:1–34.
[99] Simpson J. Gravity currents: in the environment and the laboratory. In the Environment and the Lab. Cambridge University Press; 1999. ISBN 9780521664011
[100] Smagorinsky J. General circulation experiments with the primitive equations: I. the basic experiment. Mon Weather Rev 1963;91(3):99–164.
[101] Sun G, Domaradzki JA. Implicit LES using adaptive filtering. J Comput Phys 2018.
[102] Tadmor E. Convergence of spectral methods for nonlinear conservation laws. SIAM J Numer Anal 1989;26(1):30–44.
[103] Tokyay T, Constantinescu G. The effects of a submerged non-erodible triangular obstacle on bottom propagating gravity currents. Phys Fluids 2015;27(5):056601.
[104] Tokyay T, Constantinescu G, Meiburg E. Lock-exchange gravity currents with a high volume of release propagating over a periodic array of obstacles. J Fluid Mech 2011;672:570–605.
[105] Tokyay T, Constantinescu G, Meiburg E. Tail structure and bed friction velocity distribution of gravity currents propagating over an array of obstacles. J Fluid Mech 2012;**694**:252–91.
[106] Tokyay T, Constantinescu G, Meiburg E. Lock-exchange gravity currents with a low volume of release propagating over an array of obstacles. J Geophys Res Oceans 2014;119(5):2752–68.
[107] Tseng Y-h, Ferziger JH. Mixing and available potential energy in stratified flows. Phys Fluids 2001;13(5):1281–93.
[108] Venayagamoorthy S, Koseff J, Ferziger J, Shih L. Testing of RANS turbulence models for stratified flows based on DNS data. Tech. Rep.. Standford University; 2003.
[109] Vreman AW. An eddy-viscosity subgrid-scale model for turbulent shear flow: algebraic theory and applications. Phys Fluids 2004;16(10):3670–81.
[110] Vreman B, Geurts B, Kuerten H. Comparison of numerical schemes in large-eddy simulation of the temporal mixing layer. Int J Numer Methods Fluids 1996;22(4):297–311.
[111] Wilson RI, Friedrich H, Stevens C. Flow structure of unconfined turbidity currents interacting with an obstacle. Environ Fluid Mech 2018;18(6):1571–94.
[112] Winters KB, Lombard PN, Riley JJ, D'Asaro EA. Available potential energy and mixing in density-stratified fluids. J Fluid Mech 1995;289:115–28.
[113] Yalin M, Karahan E. Inception of sediment transport. J Hydraul Div 1979;105(11):1433–43.
[114] Zemach T, Ungarish M, Martin A, Negretti M-E. On gravity currents of fixed volume that encounter a down-slope or up-slope bottom. Phys Fluids 2019;31(9):096604.
[115] Zgheib N, Bonometti T, Balanchandar S. Direct numerical simulation of cylindrical particle-laden gravity currents. Comput Fluids 2015;123:23–31.
[116] Zhou Y. Rayleigh–Taylor and Richtmyer–Meshkov instability induced flow, turbulence, and mixing. I. Phys Rep 2017;720:1–136.
[117] Zhou Y. Rayleigh–Taylor and Richtmyer–Meshkov instability induced flow, turbulence, and mixing. II. Phys Rep 2017;723:1–160.
[118] Zhou Y, Clark TT, Clark DS, Gail Glendinning S, Aaron Skinner M, Huntington CM, et al. Turbulent mixing and transition criteria of flows induced by hydrodynamic instabilities. Phys Plasmas 2019;26(8):080901.